

Πανεπιστήμιο Κρήτης  
Σχολή Θετικών και Τεχνολογικών Επιστημών  
Τμήμα Φυσικής

Μ.Π.Σ.  
Μικροηλεκτρονικής - Οπτοηλεκτρονικής

Χαρακτηρισμός της ευαισθησίας  
και ποσοτικοποίηση της Τομογραφίας  
Φθορισμού

Ψυχαράκης Στυλιανός

Ηράκλειο 2008



# Table of Contents

	<b>Chapter 1: Introduction .....</b>	3
1.1	The general Idea.....	4
	<b>Chapter 2: The Diffusion Equation .....</b>	7
2.1	Flux Conservation.....	8
2.1.1	Optical Properties.....	9
2.2	Diffusion Equation.....	13
2.3	The excitation source term.....	14
2.4	The Fluorescence source term.....	15
2.5	The Born Approximation.....	17
	<b>Chapter 3: The effects of boundaries .....</b>	18
3.1	Boundary conditions for planar interfaces.....	19
3.2	Free space propagation.....	22
3.3	From finite to infinite volumes.....	23
	<b>Chapter 4 : Inverse Problem.....</b>	26
4.1	The Normalized Born algorithm.....	27
4.2	Weight Matrix.....	28
4.3	ART.....	29
	<b>Chapter 5: Material and Methods.....</b>	32
5.1	Tissue-like phantoms.....	33
5.1.1	Preparation of phantoms.....	35
5.1.2	Mice.....	37
5.3	Experimental Setup.....	38
	<b>Chapter 6 : Experiments &amp; Results.....</b>	42
6.1	Experimental procedure.....	42
6.1.1	Data collection.....	42
6.1.2	Data Processing.....	44
6.2	Experiments and Results.....	46
6.2.1	Quantification.....	46
6.2.2	Resolution experiments.....	51
6.2.3	Spectral Unmixing.....	55
	<b>Chapter 7: Conclusions and Future outlook.....</b>	63
	References.....	66



# Chapter 1

## Introduction

The study of light transport through high scattering media, such as biological tissue, has been a topic of interest for decades in several different disciplines. This has been motivated by the fact that light offers unique contrast mechanisms while probing structural and functional characteristics. Furthermore, the low cost and the nonionizing nature of the radiation are also important incentives towards this research field.

Lately, rigorous mathematical modelling of light propagation in tissue, combined with technological advancements in photon sources and detection techniques has established optical tomography as one of the main tomographic modalities applied to molecular imaging studies. Molecular imaging can be defined as the application of non-invasive techniques for the visualization of molecular events in the cellular or subcellular level, inside intact living systems.

Fluorescence Molecular Tomography (FMT) incorporates the principles of Diffuse Optical Tomography (DOT) with the use of fluorescent probes as a source of contrast [1-7] In FMT the subject that carries the fluorescent probe is exposed to light from different source positions and the emitted light is captured by detectors arranged in a spatially defined order, either on reflectance or transmittance geometry. The accumulated information is then mathematically processed, resulting in a reconstructed tomographic image.

The fluorescence molecular tomographer, that is presented in this thesis has already been implemented and applied to several cases of small animal imaging with satisfactory results. Specific functional characteristics or whole organs have been

imaged with quite satisfactory results.. The aim of the work presented in this thesis, though, is to test the system under more controlled conditions. The experiments dealt mainly with tissue phantoms in order to establish the sensitivity and resolution of the setup, by using subjects with a priori known fluorophores' concentration and optical properties. We have also made an approach study about different spectral data unmixing autofluorescence removal from fluorescing samples, i.e. we tried to eliminate the emitted light from the medium surrounding the fluorophores, lessening thus the contrast and the quality of the imaging results.

## 1.2 The general idea

The general scheme of an ideal non-contact fluorescence imaging setup can be seen in Figure 1.1. Although it seems overly simplistic, it presents the core of the whole process. It describes the basic outlines of a rather complicated theory, applied though in a compact and easy to use experimental setup that gives us information about the spatial and quantitative distribution of light emitting objects(organs) buried inside a highly scattering medium (biological tissue)[8, 9].

As can be seen in Fig. 1.1, a laser beam of wavelength  $\lambda_a$  illuminates a highly scattering medium containing fluorophores. This can be either a tissue phantom that have different shapes or a biological sample (e.g. a mouse). The light propagates inside the medium and excites the fluorophores that are placed there. Upon excitation the fluorophores act as secondary sources and they emit light of different wavelength  $\lambda_b$ . A CCD camera, focused on the surface of the imaging sample, records either the fluorescence or the excitation light emerging from the boundary, depending on the emission filter placed in front of the camera.

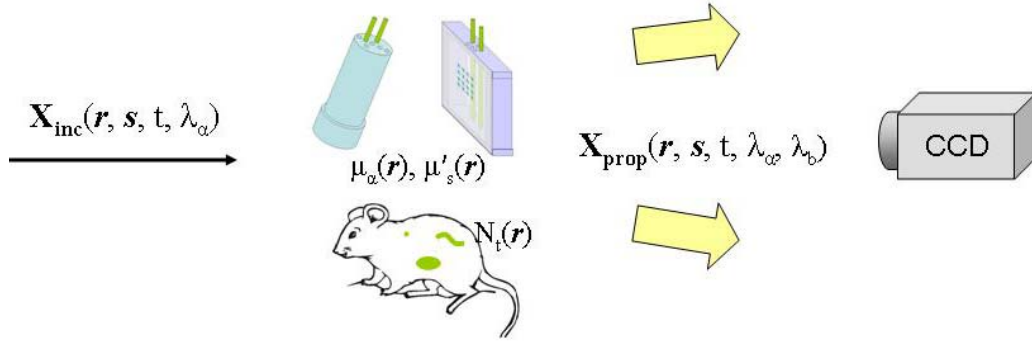


**Figure 1.1:** a simple schematic describing the experimental process

The optical tomographer has three main components, namely the source, the subject and the detector. The illumination source is usually a laser beam, and is denoted as  $X_{inc}$  of wavelength  $\lambda_a$ , in a position  $\mathbf{r}$ , propagating along a direction  $\mathbf{s}$ , with an intensity that may depends on time  $t$ . The object of volume  $V$  is turbid and in general an inhomogeneous medium which contains fluorophores whose concentration is denoted as  $N_f(\mathbf{r})$ . It is assumed that both optical properties, i.e. the absorption and scattering, expressed as  $\mu_a(\mathbf{r})$  and  $\mu'_s(\mathbf{r})$  respectively, and the fluorescent concentration remain constant, or else, that they change in a time scale much longer than the propagation of light. The excitation and emission light, emerging from the surface of the object is expressed as  $X_{prop}$ .  $\hat{n}$  is the normal to the boundary pointing away from the turbid medium.

The problem of reconstructing the map of the fluorescent concentration,  $N_f(\mathbf{r})$ , spread inside turbid medium has to be divided in two parts. These are known as the forward and the inverse problem. In order to explain these two problems we will consider the description above for Figure 1.

The forward problem is, given the light source distribution  $X_{inc}$ , the optical properties of the medium  $\mu_a(\mathbf{r})$  and  $\mu'_s(\mathbf{r})$ , and the distribution of the fluorophores  $N_f(\mathbf{r})$  within  $V$ , find the light distribution  $X_{prop}$  at any position inside the medium and, therefore, on the surface  $S$ . On the other hand, the inverse problem is expressed as: given the distribution of light sources  $X_{inc}$  and the measurement of light distribution  $X_{prop}$  on surface  $S$ , derive the optical properties of the medium  $\mu_a(\mathbf{r})$  and  $\mu'_s(\mathbf{r})$ , and the distribution of the fluorophores  $N_f(\mathbf{r})$  within  $V$ . The tomographic image is obtained by

solving the inverse problem, which involves solving several times the forward problem for each possible configuration.

In this thesis the first three chapters besides the introduction describe the theoretical basis of extracting tomographic images from fluorescence tomography. Chapter 2 describes the propagation of the excitation and fluorescence light inside an infinite turbid medium. In chapter 3 the contribution of the boundaries is considered to extract the light propagation expressions that correspond to our experiments. In chapter 4 the inverse problem is described as well as the way that the fluorescence reconstructions are extracted. The materials and the experimental methods used are presented in chapter 5. Tissue like phantoms preparation and the experimental setup description are also outlined. The experimental results are presented in chapter 6. Experiments on phantoms were performed in the direction of determining important characteristics of the imaging setup. Quantification and resolution experiments as well as a study on spectral unmixing are presented. Finally, in chapter 7 the results are discussed as well as some future aspects of the experiments are described.

## Chapter 2

# The Diffusion Equation

Light propagation in biological tissue can be typically modelled through two theories; the wave theory (Maxwell equations) and the transport theory. In wave theory, we start with the Maxwell equations where we introduce the dielectric characteristics of particles, and obtain appropriate differential or integral equations for the electromagnetic field in space and time. This is mathematically rigorous in the sense that in principle all the multiple scattering, diffraction, and interference effects can be included. However, in most practical systems, extracting a solution is impossible due to the complexity of the problem.

Transport theory, on the other hand, does not start with the wave equation. In transport theory, light is treated as energy propagating through a medium containing particles[10]. The basic differential equation is called radiative transfer equation (RTE) and is equivalent to Boltzmann's equation used in the kinetic theory of gases. It is an energy conservation equation where the propagating light has gain and losses due to the scattering and absorption processes. The development of the theory is heuristic and it lacks the mathematical rigor of the wave theory. Even though diffraction and interference effects are included in the description of scattering and absorption characteristics of a single particle, transport theory itself does not include diffraction effects. It is assumed in transport theory that there is no correlation between fields, and therefore, the addition of powers rather than the addition of fields holds[11, 12].

Theoretical research in tissue optics has been traditionally based in transport theory. The propagation of incoherent photons in a scattering and absorbing medium is described by the radiative transfer equation (RTE)[11-13]:

$$\frac{n}{c} \frac{\partial I(\vec{r}, \hat{s})}{\partial t} = -\hat{s} \cdot \nabla I(\vec{r}, \hat{s}) - \mu_t I(\vec{r}, \hat{s}) + \frac{\mu_s}{4\pi} \int_{4\pi} p(\hat{s}, \hat{s}') I(\vec{r}, \hat{s}') d\Omega' + \varepsilon(\vec{r}, \hat{s}), \quad (2.1)$$

where  $n$  is the refractive index of the medium,  $c$  the speed of light in vacuum,  $p(\hat{s}, \hat{s}')$  is the *phase function*,  $I(\vec{r}, \hat{s})$  the *specific intensity* and  $d\Omega'$  is a differential solid angle in the direction  $\hat{s}'$ . As *specific intensity*  $I(\vec{r}, \hat{s})$  is defined the average power flux at the position  $\mathbf{r}$  which flows in the direction  $\hat{s}$  and has units of  $W\ cm^{-2}\ sr^{-1}$  (sr: unit of solid angle). Also in Eq. (2.1) are presented the *total macroscopic cross-section*  $\mu_t$ , and  $\varepsilon(\vec{r}, \hat{s})$  which is the power radiated by the medium per unit volume and per unit solid angle in direction  $\hat{s}$ .

The RTE can be thought as a conservation equation for the average intensity. If we consider a small volume element around a position  $\mathbf{r}$ , in the direction  $\hat{s}$ , the left hand side of the equation accounts for photons leaving the small element, and the right hand side accounts for photons entering the small volume element. The term on the left-hand side is the time-derivative of the specific intensity which equals the number of photons entering minus the number of photons leaving the volume element. The first term on the right-hand side accounts for the flux of photons along the direction  $\hat{s}$ . The second term accounts for the scattering and absorption of photons within the infinitesimal volume element. Photons travelling along  $\hat{s}$  that are scattered from an element are balanced by the scattering into another element in the medium. The balance is handled by the integral on the right-hand side of Eq.(2.1) which accounts for photons at position  $\mathbf{r}$  being scattered from all directions  $\hat{s}'$  into direction  $\hat{s}$ . The last term on the right-hand side is the source of photons.

## 2.1 Flux conservation

If we integrate over all  $4\pi$  of solid angle in the RTE, Eq.(2.1), we obtain:

$$\frac{1}{c} \frac{\partial}{\partial t} \int_{4\pi} I(\mathbf{r}, \hat{s}) d\Omega = -\nabla \cdot \int_{4\pi} I(\mathbf{r}, \hat{s}) \hat{s} d\Omega - \mu_a \int_{4\pi} I(\mathbf{r}, \hat{s}) d\Omega + \int_{4\pi} \varepsilon(\mathbf{r}, \hat{s}) d\Omega \quad (2.2)$$

In Eq.(2.2) can recognise some interesting radiometric quantities: the *average Intensity*  $U$  and the *total flux density*  $\mathbf{J}$ , both measured in  $W/cm^2$ , which are defined in terms of the specific Intensity:

$$U(\mathbf{r}) = \int_{4\pi} I(\mathbf{r}, \hat{s}) d\Omega \quad (2.3)$$

$$\mathbf{J}(\mathbf{r}) = \int_{4\pi} I(\mathbf{r}, \hat{s}) \hat{s} d\Omega \quad (2.4)$$

By replacing Eq.(2.3) and Eq.(2.4) in Eq.(2.2) , we obtain the following equation, which is the equation of *flux conservation*:

$$\frac{1}{c} \frac{\partial U(\mathbf{r})}{\partial t} + \nabla \cdot \mathbf{J}(\mathbf{r}) + \mu_a U(\mathbf{r}) = E(\mathbf{r}), \quad (2.5)$$

In Eq. (2.5) we define:

$$E(\mathbf{r}) = \int_{4\pi} \varepsilon(\mathbf{r}, \hat{s}) d\Omega \quad (2.6)$$

which is the Source term and represents the power generated per unit volume [W/cm<sup>3</sup>].

## 2.1.1 Optical Parameters

In this section we have gathered optical parameters that are important for describing and understanding light propagation in biological tissue or tissue-like samples. These quantities are here presented and discussed.

We will start with the *total macroscopic cross-section*  $\mu_t$  [cm<sup>-1</sup>] describes the probability that a photon gets either scattered or absorbed per unit length of its travel in the medium. It is also called *transport coefficient*, or *total attenuation coefficient* and is defined as:

$$\mu_t = \rho \sigma_t = \rho(\sigma_a + \sigma_s), \quad (2.7)$$

In the above equation,  $\rho$  is the density of scatterers, and  $\sigma_a$ ,  $\sigma_s$ ,  $\sigma_t$  are the absorption, scattering and attenuation cross-sections, respectively, all of them measured in cm<sup>2</sup>. The transport coefficient can also be written as:

$$\mu_t = \mu_a + \mu_s, \quad (2.8)$$

where  $\mu_a$  and  $\mu_s$  are the absorption and scattering coefficients respectively. In terms of  $\mu_s$ , we define the *scattering mean free path*  $l_{sc}$  (or just mean free path) as:

$$l_{sc} = \frac{1}{\mu_s}, \quad (2.9)$$

which stands for the mean distance that a photon travels between two scattering events.

Similarly to the scattering mean free path, the absorption length  $\mu_a$  is defined in terms of the absorption coefficient as:

$$l_a = \frac{1}{\mu_a}. \quad (2.10)$$

The absorption length describes the average distance that a photon travels before it is absorbed, or, statistically, represents the distance at which the light intensity decreases by a factor of e, that is  $I \propto \exp[-\mu_a |r|]$ .

Another quantity that characterises the scattering properties of a medium is the (*scattering*) *phase function*  $p(\hat{s}, \hat{s}')$ . It is, actually, a probability density function and represents the probability that a photon propagating in direction  $\hat{s}$  can be scattered into a direction  $\hat{s}'$ . The phase function holds the following relationship:

$$\frac{1}{4\pi} \int_{4\pi} p(\hat{s}, \hat{s}') d\Omega = \frac{\mu_s}{\mu_t} = \frac{\sigma_s}{\sigma_t} = W_0 \quad (2.11)$$

where  $W_0$  is the albedo of a single particle, a quantity that represents the “whiteness” of a particle, therefore its capability to scatter light. The phase function can also be defined in such a way that its solid angle integral Eq. (11) is equal to one, i.e. normalize  $p(\hat{s}, \hat{s}')$  to the albedo.

In biological tissues a general assumption is that the phase function  $p(\hat{s}, \hat{s}')$  depends only on the angle between the vectors  $\hat{s}$  and  $\hat{s}'$ , as light scattering is considered to be symmetric to the direction of incidence. So we can write  $p(\hat{s}, \hat{s}') = p(\hat{s} \cdot \hat{s}') = p(\cos \theta)$ . The phase function can often be approximated by the following form

$$p(\cos \theta) = \frac{W_0(1 - g^2)}{(1 + g^2 - 2g \cos \theta)^{3/2}} \quad (2.12)$$

which is the well-known Henyey-Greenstein formula, and constitutes the most commonly used approximation for the phase function in biomedical media. In Eq2.12,  $g$  is the average cosine of the scattering angle,  $\theta$ , and it is defined in terms of the phase function:

$$g = \langle \cos \theta \rangle = \frac{\int_{4\pi} p(\hat{s} \cdot \hat{s}') \hat{s} \cdot \hat{s}' d\Omega'}{\int_{4\pi} p(\hat{s} \cdot \hat{s}') d\Omega'} \quad (2.13)$$

Therefore  $g$  is a quantity which expresses the anisotropy of the scattered light on interaction with the particle, and, as such, is called the *anisotropy factor*. Anisotropy factor  $g$  takes values from -1 to 1, for complete backscattering and forward scattering respectively; when  $g = 0$  we have isotropic scattering.

In terms of  $\mu_s$ , we also define the *reduced scattering coefficient*  $\mu'_s$ , which takes into account the anisotropy of scattered light:

$$\mu'_s = \mu_s \cdot (1 - g) \quad (2.14)$$

Through  $\mu'_s$  we define the *transport mean free path*  $l_{tr}$ , which also includes the anisotropy factor  $g$ :

$$l_{tr} = \frac{1}{\mu'_s} = \frac{l_{sc}}{1 - g} \quad (2.15)$$

The reduced scattering coefficient is the reciprocal of the mean random-walk step. The significance of this term can be understood by assuming two limiting cases, when scattering is fully isotropic and when scattering is fully anisotropic. In the first case,  $g = 0$  and Eq 2.15 gives us  $l_{tr} = l_{sc}$ . This means that the radiation can be scattered to any direction after travelling one scattering mean free path  $l_{tr}$ . On the other hand, when scattering is fully anisotropic, then  $g \sim 1$  and  $l_{tr} \sim \infty$ . This means that the radiation travels large distances without changing its direction. Therefore the transport mean free path ( $1/\mu'_s$ ) can be understood as the average distance that a photon travels before its propagation direction is completely randomized by series of scattering events. In other words,  $1/\mu'_s$  defines the average distance where the scattering can be regarded as isotropic and the propagating radiation as diffuse.

## 2.2 Diffusion Equation

The use of RTE for tissue measurements imposes several practical limitations due to its integral-differential nature. Therefore approximations have been developed to convert the transport equation to more manageable but functional forms[14, 15]. In a highly scattering medium the directions of photons are randomized after a few scattering events. Under these conditions the average intensity is only weakly anisotropic and the radiative transport equations can be simplified to a photon diffusion equation.

A standard approach expands the specific intensity  $I$  in a series of spherical harmonics. Truncation of the series at  $N$  terms can simplify the transport equation and is denoted as the  $P_N$  approximation. If this expansion is truncated at the first term, this consists the  $P_1$  approximation:

$$I(\mathbf{r}, \hat{\mathbf{s}}) \approx \frac{U(\mathbf{r})}{4\pi} + \frac{3}{4\pi} J(\mathbf{r}) \cdot \hat{\mathbf{s}} \quad (2.16)$$

The  $P_1$  approximation is quite good when the albedo  $W_0 \sim 1$ , the phase function is not too anisotropic, and the source-detector separation is large compared to  $l_{tr}$ .

If we substitute Eq. 2.16 into the time-dependent expression for the RTE, we reach the following expression for an *isotropic*<sup>1</sup> source in a medium with absorption coefficient  $\mu_a$ , reduced scattering coefficient  $\mu'_s$  and index of refraction  $n_0$ :

$$\nabla U(\mathbf{r}, t) = -3\mu'_s \left[ \frac{n_0}{c\mu'_s} \left( \frac{\partial}{\partial t} + \frac{c\mu_a}{n_0} \right) + 1 \right] \mathbf{J}(\mathbf{r}, t) \quad (2.17)$$

In Eq. 2.17 we find two terms that have units of time,

$$t_w = \frac{n_0}{c\mu'_s} = \frac{n_0}{c} l_w, \quad (2.18)$$

which represents the average time required for  $\mathbf{J}$  to travel one mean transport path distance, and

$$t_a = \frac{n_0}{c\mu_a}, \quad (2.19)$$

which is the characteristic time needed for flux  $\mathbf{J}$  to change due to absorption.

Apart from the isotropic source, diffusion approximation makes another important assumption. We assume that variations in the diffuse total flux take place over a time scale much larger than the lapse between scattering events on particles of the medium, and also, that the time of change of the total flux due to absorption is much larger than the time between scattering events. This means that we can neglect the term  $(\partial / \partial t + \mu_a c / n)$  in Eq (2.17). Hence by solving for the total flux  $\mathbf{J}$  we obtain:

$$\mathbf{J}(\mathbf{r}) = -\frac{1}{3\mu'_s} \nabla U(\mathbf{r}), \quad (2.20)$$

which is the *Fick's law* for the diffusion of the average intensity.

The coefficient in Eq (2.18) that relates  $\nabla U$  and  $\mathbf{J}$  is called the *diffusion coefficient*  $D$ , it has units of  $\text{cm}^{-1}$  and it is defined as[16]:

$$D = \frac{1}{3\mu'_s} = \frac{1}{3\mu_s(1-g)} = \frac{l_w}{3}. \quad (2.21)$$

By substituting the expression for  $\mathbf{J}$  from Fick's law, into the general expression for flux conservation, eq. (2.5), we obtain the *diffusion equation (D.E.)*:

$$\frac{1}{c} \frac{\partial U(\mathbf{r})}{\partial t} - D \nabla^2 U(\mathbf{r}) + \mu_a U(\mathbf{r}) = E(\mathbf{r}) + \nabla D \cdot \nabla U(\mathbf{r}) \quad (2.22)$$

---

<sup>1</sup> i.e. the incident intensities in Eq. (2.6) do not depend on  $\hat{s}$

In an infinite homogenous medium in which both  $D$  and  $\mu_a$  are constant throughout the medium, the diffusion equation reduces to the most common expression:

$$\frac{1}{c} \frac{\partial U(\mathbf{r})}{\partial t} - D \nabla^2 U(\mathbf{r}) + \mu_a U(\mathbf{r}) = E(\mathbf{r}) \quad (2.23)$$

Suppose now that we have a continuous source of photons at some point  $\mathbf{r}_s$ . In this case, the solution to Eq (2.23) is:

$$U(\mathbf{r}) \propto \exp\left[-\frac{|\mathbf{r} - \mathbf{r}_s|}{L_d}\right] \quad (2.24)$$

where we have defined the diffusion length  $L_d$  as:

$$L_d = \sqrt{\frac{D}{\mu_a}} \quad (2.25)$$

At this point we refer concisely to the assumptions followed in order to derive the diffusion equation. First of all, the diffusion approximation assumes that there is high concentration of scatterers inside the medium, so that the propagating photons have undergone multiple scattering events and light is considered highly incoherent and diffuse. In order to derive Eq.(2.23) we assumed that a homogenous medium, meaning that  $\mu'_s$ ,  $\mu_a$  as well as  $D$  are constant throughout the medium. We have also assumed that the medium was illuminated by isotropic sources and finally that the variations of the total flux (including variations due to absorption) occur in a time scale much larger than the time between the scattering events.

## 2.2.1 Solutions of the Diffusion Equation for infinite homogeneous media

Although tomography deals with objects of finite dimensions, it is useful to find first the solution for the case of an infinite medium. Later on, a more realistic expression will be presented, which will take into consideration also the contribution of the boundaries of the object.

As we already have described in Chapter 1, there are two sources of light; the laser source of wavelength  $\lambda_a$  that illuminates the medium and the fluorescent molecules that emit light of wavelength  $\lambda_b$ , after being excited by the diffuse excitation light of wavelength  $\lambda_a$ . In this section we will derive the expressions for the

propagation of the excitation and the emission light inside the medium by applying the appropriate source term to the diffusion equation in each case. For our convenience we rewrite the diffusion equation:

$$\frac{1}{c} \frac{\partial U(\mathbf{r}, t)}{\partial t} - D \nabla^2 U(\mathbf{r}, t) + \mu_a U(\mathbf{r}, t) = E(\mathbf{r}, t) \quad (2.26)$$

This standard diffusion equation can be transformed into a Helmholtz equation by decomposing  $\partial U / \partial t$  into frequencies.

### 2.3 The Excitation Source term

The form of the Helmholtz equation depends on the light source used. Let us consider a continuous wave (cw) laser source irradiating the sample of Fig1.1. A common way of defining the source within a scattering medium is to consider a point source located at  $z \sim l_{tr}$  inside the medium. In order to describe the source term we use a delta function. This delta function implies isotropic emission of light of strength  $S_0$ . Therefore the source term of Eq. (2.26) can be written as:

$$E(\mathbf{r}, t) \rightarrow S_0 \cdot \delta(\mathbf{r}) \quad (2.27)$$

If we replace Eq.(2.27) in Eq.(2.26) the diffusion equation for the average intensity obeys the following equation which has the form of a modified Helmholtz equation:

$$\nabla^2 U(\mathbf{r}) + \kappa_0^2 U(\mathbf{r}) = \frac{S_0 \cdot \delta(\mathbf{r})}{D} \quad (2.28)$$

where  $\kappa_0$  is the wavenumber:

$$\kappa_0 = i \sqrt{\frac{\mu_a}{D}} \quad (2.29)$$

The Helmholtz equation can be solved with the use of Green's functions. Therefore, in infinite medium the Green function  $G$  satisfies [17]:

$$\nabla^2 G(\kappa | \mathbf{r} - \mathbf{r}_s |) + \kappa_0^2 G(\kappa | \mathbf{r} - \mathbf{r}_s |) = -4\pi \cdot \delta(\mathbf{r} - \mathbf{r}_s) \quad (2.30)$$

where  $\mathbf{r}_s$  stands for the source points, and the solution to it, is

$$G(\kappa | \mathbf{r} - \mathbf{r}_s |) = \frac{\exp(i\kappa_0 | \mathbf{r} - \mathbf{r}_s |)}{|\mathbf{r} - \mathbf{r}_s |} \quad (2.31)$$

For the case of a point source, the distribution of the average Intensity in an infinite homogenous medium is given as:

$$U^{exc}(\mathbf{r}) = \frac{S_0}{4\pi D} \frac{\exp(i\kappa_0 |\mathbf{r} - \mathbf{r}_s|)}{|\mathbf{r} - \mathbf{r}_s|} \quad (2.32)$$

If we consider the more general case of a source term with spatial distribution  $E(\mathbf{r}, t) = S(\mathbf{r})$ , then the solution of the diffusion equation is the following:

$$U^{exc}(\mathbf{r}) = \frac{1}{4\pi D} \int_V \frac{S(\mathbf{r}') \cdot \exp(i\kappa_0 |\mathbf{r} - \mathbf{r}'|)}{|\mathbf{r} - \mathbf{r}'|} dV \quad (2.33)$$

## 2.4 The Fluorescent Source term

After we have solved the diffusion equation for the excitation source and we have expressed the average density  $U(\mathbf{r})$  that propagates inside the medium, the next step is to find an expression for the propagating emitted fluorescent light. The incident light of wavelength  $\lambda_a$  propagates inside the tissue in a diffuse way and excites the fluorescent particles which will emit photons of different wavelength  $\lambda_b$ . The fluorescent photons travel also in a diffuse way inside the medium.

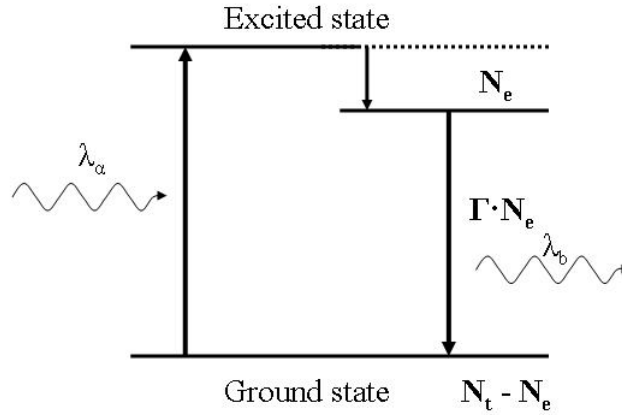


**Figure 2.1:** emission in a two-states system

In order to obtain an expression for the fluorescent propagating light, we solve the diffusion equation Eq.(2.26) by applying to it the appropriate expression for the fluorescent source term. We approximate the fluorophores as two-level systems and we also assume that the surrounding medium has no gain. The number of excited molecules per unit volume is given by the following rate equation:

$$\frac{\partial N_e(\mathbf{r}, t)}{\partial t} = -\Gamma N_e(\mathbf{r}, t) + \sigma^{fluor} U^{exc}(\mathbf{r}, t) [N_t(\mathbf{r}, t) - 2N_e(\mathbf{r}, t)] \quad (2.34)$$

where  $N_e(\mathbf{r}, t)$  is the number of fluorescent molecules per unit volume in the excited state at position  $\mathbf{r}$  and time  $t$ ;  $N_t(\mathbf{r}, t)$  is the total number of the fluorescent molecules per unit volume (the sum of excited and ground state molecules);  $\sigma^{flu}$  is the absorption cross section of a molecule (i.e. likelihood to absorb the excitation wavelength  $\lambda_a$ );  $U^{exc}(\mathbf{r}, t)$  is the excitation average intensity (at  $\lambda_a$ ) and  $\Gamma$  is the total (radiative) decay rate from the excited state to the ground state.

For a continuous wave excitation source, as it is the case in our experimental setup, we reach a steady state ( $\partial N_e / \partial t = 0$ ). Therefore, we can solve Eq.(2.34) for the emitted molecules density number:

$$N_e(\mathbf{r}, \mathbf{r}_s) = \frac{\sigma^{flu} N_t(\mathbf{r}, \mathbf{r}_s)}{\Gamma + 2\sigma^{flu} U^{exc}(\mathbf{r}, \mathbf{r}_s)} U^{exc}(\mathbf{r}, \mathbf{r}_s) \quad (2.35)$$

Typical values of the absorption cross section are in the order of  $10^{-6} \text{ cm}^2$ . The fluorescence lifetime for the fluorophores used is in the order of nanoseconds, so  $\Gamma \sim 10^9$ . For intensities in the order of  $\sim mW/cm^2$ , which is the case in our experiments,  $\Gamma \gg 2\sigma^{flu} U^{exc}(\mathbf{r}, \mathbf{r}_s)$  and, hence, Eq. 2.35 is simplified:

$$N_e(\mathbf{r}, \mathbf{r}_s) = \frac{\sigma^{flu} N_t(\mathbf{r}, \mathbf{r}_s)}{\Gamma} U^{exc}(\mathbf{r}, \mathbf{r}_s) \quad (2.36)$$

Therefore, the source term of the fluorescent light which represents the number of fluorescent photons emitted per unit volume per second is

$$S^{flu}(\mathbf{r}, \mathbf{r}_s) = \Gamma \eta N_e(\mathbf{r}, \mathbf{r}_s) = \eta \sigma^{flu} N_t(\mathbf{r}, \mathbf{r}_s) U^{exc}(\mathbf{r}, \mathbf{r}_s) \quad (2.37)$$

where  $\eta$  is the fluorescence quantum yield.

The fluorescent radiation is assumed to be well separated in energy from that of incident photons, so that we can safely ignore the possibility of the excitation of the fluorophores by the emitted fluorescent light. The fluorescent light distribution is given by the diffusion equation for the fluorescent wavelength  $\lambda_b$ , assuming a weakly absorbing spatial distribution of fluorophores (Born Approximation). The propagation of the fluorescent light can be determined over the contributions from all fluorophores [18].

$$U^{flu}(\mathbf{r}) = \frac{\sigma^{flu} \eta}{4\pi D_b} \int_V N_t(\mathbf{r}_1) U^{inc}(\mathbf{r}_1, \mathbf{r}_s) \frac{\exp(-\kappa_b |\mathbf{r} - \mathbf{r}_1|)}{|\mathbf{r} - \mathbf{r}_1|} dV_1 \quad (2.38)$$

where  $\kappa_b = \sqrt{\frac{\mu_a^{\lambda_b}}{D^{\lambda_b}}}$ , i.e.  $\mu_a$  and  $D$  that refer to the second (emitted) wavelength  $\lambda_b$ .

we can write the last equation in terms of the Green's function:

$$U^{fluo}(\mathbf{r}) = \frac{\sigma^{fluo} \eta}{4\pi D_b} \int_V N_t(\mathbf{r}) U^{inc}(\mathbf{r}_I, \mathbf{r}_s) G(\kappa_{0b} |\mathbf{r} - \mathbf{r}_I|) dV_1 \quad (2.39)$$

where  $\kappa_{0b} = i\kappa_b$ . Finally, by replacing  $U^{inc}(\mathbf{r}, \mathbf{r}_s)$  in Eq.(2.39) from Eq.(2.32) we obtain

$$U^{fluo}(\mathbf{r}) = \frac{\sigma^{fluo} \eta S_0}{16\pi^2 D_a D_b} \int_V \frac{\exp(-\kappa_a |\mathbf{r}_I - \mathbf{r}_s|)}{|\mathbf{r}_I - \mathbf{r}_s|} N_t(\mathbf{r}_I) \frac{\exp(-\kappa_b |\mathbf{r} - \mathbf{r}_I|)}{|\mathbf{r} - \mathbf{r}_I|} dV_1 \quad (2.40)$$

As it is obvious from the analysis above, the fluorescent field is a superposition of two fields with different wavenumbers  $\kappa_a$  and  $\kappa_b$ , that correspond to the excitation and the emission wavelength, respectively. The last equation can be rewritten in a more general form, in terms of Green's functions:

$$U^{fluo}(\mathbf{r}) = \frac{\sigma^{fluo} \eta S_0}{16\pi^2 D_{exc} D_{fluo}} \int_V G_{exc}(\mathbf{r}, \mathbf{r}_s) N_t(\mathbf{r}_I) G_{fluo}(\mathbf{r}, \mathbf{r}_I) dV_1 \quad (2.41)$$

where we have replaced the subscripts  $a$  and  $b$  with the more meaningful *exc* and *fluo* respectively.

## 2.5 The Born Approximation

In the previous sub-section, in order to derive the excitation light propagation and the following fluorophores excitation, we assumed a weakly absorbing spatial distribution of fluorophores. We usually write the intensity that excites the fluorophores as the sum of the scattered intensity,  $U^{sc}(\mathbf{r}, \mathbf{r}_s)$ , that reaches the fluorophores after being scattered by other absorbers and incident intensity which is the intensity that would be present in point  $\mathbf{r}$ , in the absence of the fluorophores.

$$U^{exc}(\mathbf{r}, \mathbf{r}_s) = U^{inc}(\mathbf{r}, \mathbf{r}_s) + U^{sc}(\mathbf{r}, \mathbf{r}_s) \quad (2.42)$$

In the Born approximation we do not consider the non-linear effect that the presence of the other fluorophores causes on the excitation Intensity. We assume that the fluorophores' absorption is very low and it does not affect the intensity of the propagating excitation light. Therefore we make the assumption that the average intensity incident on the fluorophores is the same as in the absence of fluorescent and absorbing sources<sup>2</sup>:

$$U^{exc}(\mathbf{r}, \mathbf{r}_s) \approx U^{inc}(\mathbf{r}, \mathbf{r}_s) \quad (2.43)$$

---

<sup>2</sup> This assumption reminds us the basic assumption of the diffusion theory, i.e. the highly scattering medium

# Chapter 3

## The effects of boundaries

In order to solve the forward problem, as stated in Chapter 1, we have to derive the expressions that describe light distribution in every phase of its propagation from the source to the detector. Up to this point, we have studied light propagation inside a turbid, highly scattering medium. We have presented the diffusion equation and we have derived the corresponding expressions for the propagating incident ( $\lambda_a$ ) and fluorescent light ( $\lambda_b$ ), Eq.(2.32) and Eq.(2.41), respectively. However, this is for the case of an infinite diffusive medium. Another important issue that has to be considered is the shape of the volume  $V$ , as incident photons are expected to interact with the surface of the object. In the basic experimental scheme of Figure 1.1, the surface of the subject has an arbitrary shape, depending on the sample. In order to find a solution at the surface of the medium, we introduce certain conditions that have to be fulfilled on these separating surfaces, the so called *boundary conditions*.

For the case of a biologic medium the surface separates the tissue whose index of refraction is approximated with that of water,  $n_{in} \sim 1.333$  and air, whose index of refraction is  $n_{out} = 1$ .

Therefore, in order to derive the expressions that correspond to the real situation, we have to account for the contribution of the surface to light propagation for a subject that has a finite volume.

### 3.1 Boundary conditions for planar interfaces

The work presented in this thesis deals mostly with planar tissue-like phantoms. In the first section of this chapter the expressions for light distribution at any position inside a semi-infinite homogeneous medium will be derived. After that, we will present the expressions for the case of a finite, homogeneous, diffuse slab, which was actually the real situation in our experiments. The geometry of the problems is illustrated in Fig. 3.1 and 3.2.

Within the diffusion approximation the exact boundary for an index mismatched boundary is that the component of the flux normal to the interface, pointing from the non-scattering medium into the turbid medium, must be zero [19].

$$\mathbf{J}_{in}(\mathbf{r}) = 0 \quad (3.1)$$

In the case where the turbid medium is bounded by a transparent medium and their refractive indices are substantially different then we must consider all possible Fresnel reflections at the interfaces from the flux inside the turbid medium. The zero-flux condition must also be considered and therefore it is assumed that all the flux traversing the interface is toward the non-diffusive medium

$$\mathbf{J}_{out}(\mathbf{r}) = \mathbf{J}_n(\mathbf{r}) \quad (3.2)$$

The methodology applied, is to employ a series of dipoles (pairs of a positive and negative source) [20] that effectively set the flux to zero at the two boundaries assumed for the two planar interfaces.

As we presented in chapter 2, the solution of the diffusion equation for a continuous wave (cw) laser source, described by a delta function  $E(\mathbf{r})=S_0\delta(\mathbf{r})$ , in an infinite medium, is given by the following Green's function, eq.(2.32):

$$U^{exc}(\mathbf{r}) = \frac{S_0}{4\pi D} \frac{\exp(i\kappa_0 |\mathbf{r} - \mathbf{r}_s|)}{|\mathbf{r} - \mathbf{r}_s|} \text{ where } \kappa_0 = i\sqrt{\mu_a/D}$$

which is rewritten here for convenience.

In order to solve the problem posed, we make two assumptions. First of all, we assume that all the incident photons are initially scattered at a depth  $z_0$ , so that the actual source term becomes the simple delta function described above, being  $z_0$  defined as:

$$z_0 = l_{tr} = [(1 - g)\mu_s]^{-1}.$$

We also specify, as mentioned above, the boundary condition at the surface of the subject. In order to retain the continuity of light propagation (flux density) at the

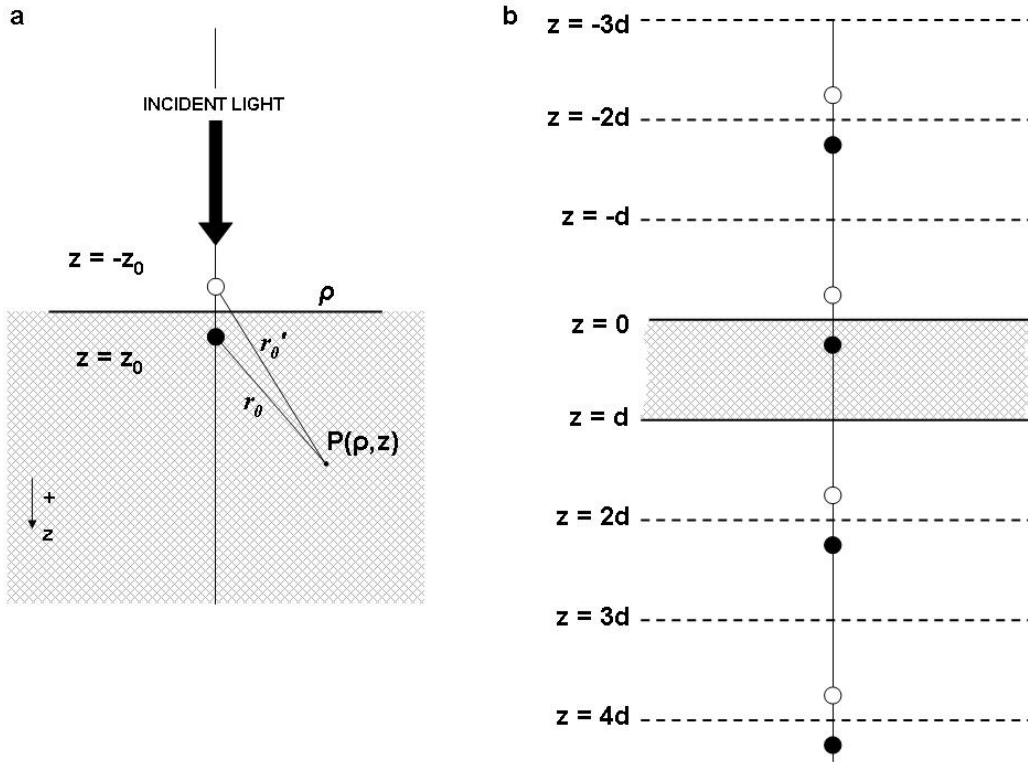


**Figure 3.1:** Source dipoles near the boundaries of (a) a semi-infinite, and (b) a finite slab of a homogeneous turbid medium.

surface, we assume that the average intensity  $U(\mathbf{r}) = 0$ , on the physical boundary  $z = 0$ . This boundary condition can be met by adding a negative or image source of photons to the infinite medium problem as shown in Fig. (3.1a) [15]. As a result, the average propagating intensity in every point inside the semi-infinite turbid medium will be calculated as the superposition of the two sources' (one positive and one negative) contributions there. Therefore, the reflectance solution for the average intensity  $U(\mathbf{r})$ , is given by the following relation:

$$U(\mathbf{r}) = \frac{S_0}{4\pi Dc} \left\{ \frac{\exp(-ikr_0)}{r_0} - \frac{\exp(-ikr_c)}{r_c} \right\} \quad (3.3)$$

where  $r_0 = \sqrt{|z - z_0|^2 + \rho^2}$  and  $r_c = \sqrt{|z + z_0|^2 + \rho^2}$ .

Generally, the boundary condition is expressed as an equation that relates  $U(\mathbf{r})$  with  $\mathbf{J}(\mathbf{r})$  at the interface.

$$U(\mathbf{r}) = C_{nd} \mathbf{J}(\mathbf{r}) \cdot \hat{\mathbf{n}} = C_{nd} J(\mathbf{r}) \quad (3.4)$$

where  $\hat{\mathbf{n}}$  is the surface normal pointing outwards the medium,  $\mathbf{J}$  is the flux vector,  $J_n$  is the total flux traversing the interface and  $C_{nd}$  is a coefficient which takes into

account the refractive index mismatch between both media. In the case of air/tissue interface  $C_{nd}$  takes values around  $\sim 5$ .

We can, thus, write the expression for the flux density

$$J(\mathbf{r}) = \frac{S_0}{4\pi cDC_{nd}} \left\{ \frac{\exp(-ikr_0)}{r_0} - \frac{\exp(-ikr_c)}{r_c} \right\} \quad (3.5)$$

Given the expression for the reflectance of a semi-infinite medium, an important question would be whether we can derive a similar expression for the transmittance through a finite turbid medium. This exactly is the case of a finite slab of thickness  $d$ , illustrated in Fig. (3.1b).

Here we have an additional boundary where the zero-flux condition must be applied. As a result, we assume that the average intensity  $U(\mathbf{r}) = 0$  also on the physical boundary  $z = d$ . This condition can be met by adding two sources near  $z = 2d$  as shown, but then the boundary condition at  $z = 0$  is violated. Both boundary conditions can be met only by adding an infinite number of dipole sources as shown in Fig. (3.1b). The number of sources required depends on the optical properties and the thickness of the slab. Usually, retaining only four dipoles suffices to satisfy the boundary conditions for practical implementations, since the contributions of additional dipoles become very small. The thicker the slab, the better this approximation performs. For thin slabs (of the order of 1cm or thinner) keeping additional dipoles may be necessary for improved accuracy.

In the case of a slab of thickness  $d$  the transmittance solution, calculated by retaining  $m$  dipoles is:

$$U(\mathbf{r}) = \frac{S_0}{4\pi Dc} \sum_{m=1}^M \left\{ \frac{\exp(-ikR_0(m))}{R_0(m)} \right\} \quad (3.6)$$

$$\text{where } R_0(m) = \left[ \left( 2\text{floor}\left(\frac{m}{2}\right)d' + (-1)^{m-1}(z - z_0) \right)^2 + \rho^2 \right]^{1/2}, \quad d' = d + z_0,$$

$\text{floor}(x)$  is the nearest integer of  $x$  towards minus infinity and  $0 < z < d$ . By applying the boundary condition Eq. (3.4), we derive the expression for the density flux for the transmittance solution:

$$J(\mathbf{r}) = \frac{S_0}{4\pi cDC_{nd}} \sum_{m=1}^M \left\{ \frac{\exp(-ikR_0(m))}{R_0(m)} \right\} \quad (3.7)$$

Depending on the kind of experiment we want to perform (e.g. shape of subject, information that we want to reconstruct), we choose the appropriate experimental geometry, that is reflectance or transmittance, which means that we use either Eq.(3.3) and Eq.(3.5) or Eq.(3.6) and Eq.(3.7) .

### 3.2 Free space propagation

The light emerging from the flat surface of our subject is being detected by a CCD camera focused on that surface. After traversing the subject, light is propagating in free space, as the surrounding medium of the subject is the air. As a result, light is not diffusive and that's why it will be described in terms of the specific Intensity.

In order to express the emerging light from a diffuse medium into free space we use the Lambert Approximation [10]. The Lambert approximation accepts that the photons emerging through a certain surface are isotropic.

Let us assume that  $S$  is the planar surface of the slab that separates the diffusive medium from the air, then the flux through the surface (exiting the slab) is:

$$J_+(\mathbf{r}) = \int_{(2\pi)^+} I(\mathbf{r}) \hat{s} \cdot \hat{s}_0 d\Omega \quad (3.8)$$

Where by integrating over  $(2\pi)^+$  we mean integration over solid angle  $2\pi$  in the forward range  $(0 \leq \theta \leq \frac{\pi}{2})$ ,  $\hat{s}$  is the unit vector along which  $I(\mathbf{r})$  is propagating,  $\hat{s}_0$  is the vector normal to the surface,  $\hat{s} \cdot \hat{s}_0 = \cos \theta$ .

Therefore Eq.(3.8) gives  $J_+(\mathbf{r}) \propto I(\mathbf{r})$ . If we take into

consideration the boundary condition of Eq. (3.2), we obtain an expression that relates the specific intensity in free space with the flux density on the boundary:

$$I(\mathbf{r}) = \frac{1}{\pi} J_n(\mathbf{r}) \quad (3.9)$$

In our case that the specific intensity  $I(\mathbf{r})$  is independent of the direction  $\hat{s}$ , the radiation is said isotropic. The power irradiated from the surface is isotropic as well. Consequently, the emerging power from the surface element  $dA$  located at position  $\mathbf{R}$  is given by:

$$P(R) = dS \int_{\Omega} I(R, s) \cos \theta d\Omega$$

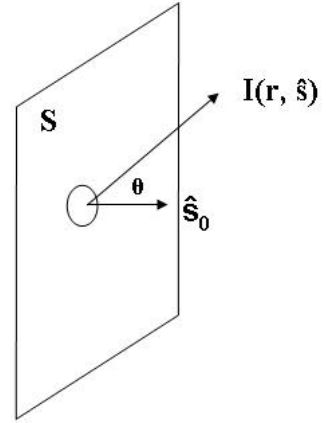


**Figure 3.2:**  
Flux through surface A

where  $\theta$  is the angle between the vector normal to  $dS$  and the vector connecting the infinitesimal emitting area with the infinitesimal detecting area. Since the camera is focused on the planar surface of the sample and there is an 1-1 direct correspondence between the emitting area  $dS$  at  $\mathbf{R}$  with the detecting infinitesimal area at  $\mathbf{R}'$ , the total power measured by a detector element (a CCD pixel for example) due to the power emerging from the sample is given as:

$$P_S(R') = \int_S \int_{\Omega} I(R, s) \cos \theta d\Omega dS = \int_S P(R) dS$$

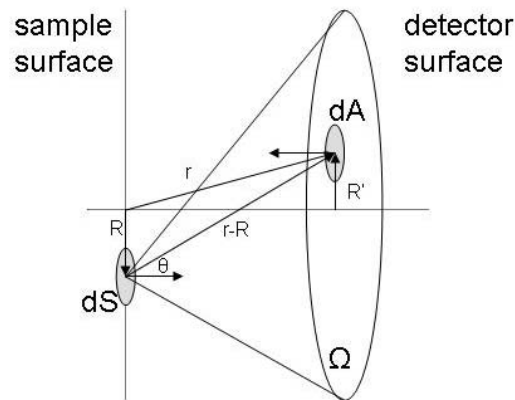


**Figure 3.3:** an infinitesimal emitting area  $dS$  and its contribution on the detector's area  $dA$

From this analysis, although it seems rather superficial, we can understand that the light emerging from the finite volume can be easily related to the signal collected by the detector, due to the free space propagation.

### 3.3 From finite to infinite volumes

The dipole approximation applied to slab phantoms mentioned above, gives satisfying results for planar samples or samples that can be considered as planar. But what would happen in case that the imaging sample had an arbitrary geometry? In this section we refer to a study [21], according to which we can obtain the tomographic “information” (i.e. the spatial distribution of the fluorescent sources) without dealing with the shape or the boundaries of the subject. Even though this method is not employed for the needs of this thesis it is presented as it vanishes the need for samples of specific shape and dimensions.

The general case (that we study in theoretical basis) consists of a diffuse medium with an arbitrary shape. It is a subject with volume  $V$ , diffusion coefficient  $D$ , absorption coefficient  $\mu_a$  and index of refraction  $n_{in}$ . If we consider the effect of the interface  $S$ , the average intensity  $U(\mathbf{r})$  inside volume  $V$  is expressed through Green's theorem:

$$U(\mathbf{r}) = U^{inf}(\mathbf{r}) - \frac{1}{4\pi} \int_S [U(\mathbf{r}') \frac{\partial G(\kappa|\mathbf{r}'-\mathbf{r}|)}{\partial \mathbf{n}'} - G(\kappa|\mathbf{r}'-\mathbf{r}|) \frac{\partial U(\mathbf{r}')}{\partial \mathbf{n}'}] dS', \quad \mathbf{r} \in V \quad (3.10)$$

where  $\mathbf{n}'$  represents the surface normal pointing outwards,  $G$  is the Green's function and the average intensity obtained in the 'infinite medium case' (i.e. absence of the surface) is:

$$U^{inf}(\mathbf{r}) = \frac{1}{4\pi D} \int_V S(\mathbf{r}') \cdot G(\kappa|\mathbf{r}'-\mathbf{r}_s|) dV \quad (3.11)$$

The last equation gives an expression for the general case of a light source with spatial distribution  $S(\mathbf{r})$ . By replacing that term with the corresponding term of either the laser source or the fluorescent molecules source term we derive the expressions for the diffuse light inside the volume.

If we rewrite eq.(3.10) in terms of flux density  $J_n$  by using the boundary condition (eq.3.4) and the Fick's law at the boundary (eq. 2.20), we get the complete expression for the flux  $J_n$  at any surface point:

$$J_n(\mathbf{r}) = \frac{1}{C_{nd}} U^{inf}(\mathbf{r}) - \frac{1}{4\pi C_{nd} D} \int_S \left[ C_{nd} D \frac{\partial G(\kappa|\mathbf{r}'-\mathbf{r}|)}{\partial \mathbf{n}'} - G(\kappa|\mathbf{r}'-\mathbf{r}|) \right] J_n(\mathbf{r}') dS', \quad \mathbf{r} \in S \quad (3.12)$$

In a similar way we can derive an analogous expression for the fluorescent light at the interface by using the boundary condition (eq.3.4). In chapter 2 we presented the average intensity of the fluorescent light in eq. (2.41) as:

$$U^{fluor}(\mathbf{r}) = \frac{\sigma^{fluor} \eta S_0}{16\pi^2 D_{exc} D_{fluor}} \int_V G_{exc}(\mathbf{r}_1, \mathbf{r}_s) N_t(\mathbf{r}_1) G_{fluor}(\mathbf{r}, \mathbf{r}_1) dV_1$$

Consequently, the fluorescence light flux on the boundary can be given by eq. (3.4):

$$J_n^{fluor}(\mathbf{r}) = \frac{\sigma^{fluor} \eta S_0}{16\pi^2 D_{exc} D_{fluor} C_{nd}} \int_V G_{exc}(\mathbf{r}_1, \mathbf{r}_s) N_t(\mathbf{r}_1) G_{fluor}(\mathbf{r}, \mathbf{r}_1) dV_1, \quad \mathbf{r} \in S \quad (3.13)$$

Given that the CCD is focused on the subject's surface, and that the flux there,  $J_n$ , is related to the measured flux,  $J_n^{meas}$ , on the detector of the camera through known relations, we can calculate average intensity created by the source distribution in the

absence of the interface. This effectively means that volume  $V$  has become infinite, filling all space with a diffusive medium of the (constant) properties of our subject ( $D$ ,  $\mu_a$ ,  $n_{in}$ ). Consequently, the infinite case average intensity is given by:

$$U^{inf}(\mathbf{r}) = C_{nd} J_n(\mathbf{r}) + \frac{1}{4\pi D} \int_S \left[ C_{nd} D \frac{\partial G(\kappa | \mathbf{r}' - \mathbf{r} |)}{\partial \mathbf{n}'} - G(\kappa | \mathbf{r}' - \mathbf{r} |) \right] J_n(\mathbf{r}') dS' \quad (3.14)$$

The study outlined above introduces a method that removes the contribution of the boundaries on the measurements, transforming the signals captured from a bounded medium to measurements that would have been obtained if no boundary were present. The main advantage of this method is that there is no need of obtaining the shape of the subject, making thus simpler and faster (in terms of computational time) the whole (image reconstructing) procedure, which is the inverse problem.

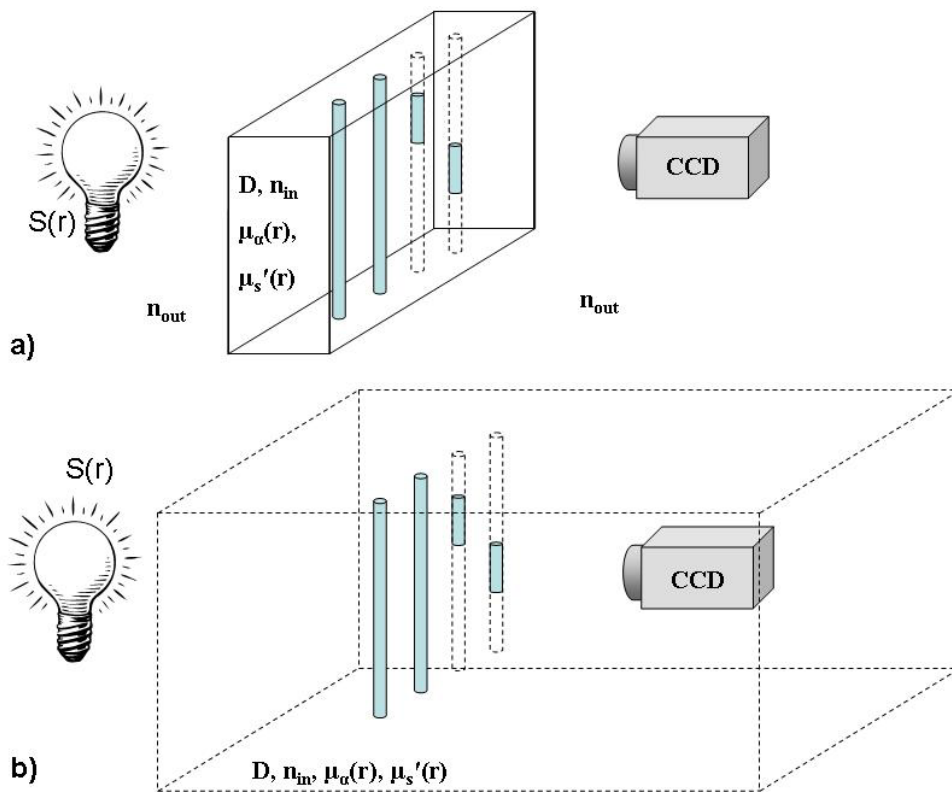


**Figure 3.4:** The effect of boundaries removal: instead of imaging a finite diffuse medium placed in a non-diffuse medium like air (a), we image a nonbounded medium avoiding thus the interfaces (b)

# Chapter 4

## Inverse problem

So far, we have dealt with the excitation and fluorescence photon waves propagation inside a diffuse medium and their interaction with the boundaries. We have described the propagation of excitation and emission light inside the medium. We have derived the corresponding solutions to the diffusion equation and we have also presented the expressions of photon flux at the interface. Therefore we have determined the light distribution inside the subject and outside of it, relating these expressions with the signal on the CCD. As a matter of fact we have set and presented the parameters of the forward problem.

In order to proceed to the reconstruction of the fluorescent sources' spatial distribution, we have to solve the inverse problem. The first thing that we have to do is to discretize the imaged volume in small elementary volumes, called voxels. After that we derive linear equations, based on the forward model, that describe the contribution of each voxel separately on the measured data, having these contributions as unknowns. The detecting area of our imaging system (CCD) will also be separated in small elementary surfaces (actually the pixels grouped into detectors of typical area sizes of 0.1 cm) and then the measured signal will be determined as the sum of the contribution of the entire subject's voxels on each pixel of the detector. This correlation will be described through a number of linear equations as it will be shown later on.

## 4.1 The normalized Born algorithm

In this section we will present a method that reconstructs the fluorescent distribution inside a homogeneous medium. The normalized Born algorithm, in general, has been proposed for reconstructing fluorescent, scattering or absorption heterogeneities in diffuse media [22, 23]. The main idea is that the algorithm is using the excitation measurement in order to specify the intrinsic properties of the subject. Therefore, the fluorescent “heterogeneities”, which are the case in our experiments, are determined by dividing the fluorescent signal measured (at wavelength  $\lambda_b$ ) by the incident excitation measurement (at wavelength  $\lambda_a$ ) as it will be demonstrated here.

In chapter 2 we described thoroughly light propagation inside a slab. If this is the case, the photon wave (or flux density) is given by Eq.(2.32). Therefore, the incident photon field detected at position  $\mathbf{r}_d$ , is:

$$U^{inc}(\mathbf{r}_s, \mathbf{r}_d) = QE^{\lambda_a} \cdot \Theta_f^{exc} \cdot \Theta_d(\mathbf{r}_d) \cdot U^{exc}(\kappa^{\lambda_b} | \mathbf{r}_s - \mathbf{r}_d |) \quad (4.15)$$

where  $QE^{\lambda_a}$  is the detector quantum efficiency at wavelength  $\lambda_a$ ,  $\Theta_f$  is the attenuation caused by the emission filter used in order to collect the excitation light,  $\Theta_d(\mathbf{r}_d)$  accounts for the detector gain and  $\kappa^{\lambda_a}$  denotes the wavenumber for the optical properties of the medium at wavelength  $\lambda_a$ .

In an analogous way we express the fluorescent light at position  $\mathbf{r}_d$ :

$$U^{fluor}(\mathbf{r}_s, \mathbf{r}_d) = QE^{\lambda_b} \Theta_f^{fluor} \Theta_d(\mathbf{r}_d) \frac{\sigma^{fluor} \eta}{4\pi D_{fluor}} \cdot \int_V U^{exc}(\kappa^{\lambda_a} | \mathbf{r} - \mathbf{r}_s |) N_t(\mathbf{r}) G_{fluor}(\kappa^{\lambda_b} | \mathbf{r}_d - \mathbf{r} |) dV \quad (4.16)$$

where  $QE^{\lambda_b}$  is the detector quantum efficiency at the emission wavelength  $\lambda_b$ ,  $\Theta_f$  is the attenuation caused by the emission filter used in order to collect the emission light,  $\kappa^{\lambda_b}$  denotes the wavenumber for the optical properties of the medium at wavelength  $\lambda_b$  and  $G(\kappa^{\lambda_b} | \mathbf{r}_d - \mathbf{r} |)$  is the Green’s function solution to the diffusion equation in a slab and describes the propagation of the emission photon wave from the fluorophore to the detector in a slab configuration.

Finding solutions for Eq. (4.2) requires determination of all position dependent factors  $\Theta_d(\mathbf{r}_d)$  for each detector. In order to obtain more manageable expressions for the fluorescence emission, we can divide Eq. (4.2) by Eq. (4.1) and rearrange the result to derive the normalized fluorescence Born measurement,  $U^{nB}$ :

$$U^{nB}(\mathbf{r}_s, \mathbf{r}_d) = \frac{U^{fluo}(\mathbf{r}_s, \mathbf{r}_d)}{U^{inc}(\mathbf{r}_s, \mathbf{r}_d)} = a \frac{\sigma^{fluo} \eta}{4\pi D_{fluo}} \cdot \frac{\int_V U^{exc}(\kappa^{\lambda a} | \mathbf{r} - \mathbf{r}_s |) \cdot N_t(\mathbf{r}) \cdot G_{fluo}(\kappa^{\lambda b} | \mathbf{r}_d - \mathbf{r} |) dV}{U^{exc}(\kappa^{\lambda b} | \mathbf{r}_s - \mathbf{r}_d |)} \quad (4.17)$$

where  $a = \frac{QE^{\lambda b} \Theta_f^{fluo}}{QE^{\lambda a} \Theta_f^{exc}}$  is a calibration factor that can be determined experimentally.

The normalized Born algorithm normalizes the fluorescent signal measured to the intrinsic properties and the heterogeneities of the subject. Another important advantage is that the position dependent terms are cancelled out, that is the filter spatial dependence.

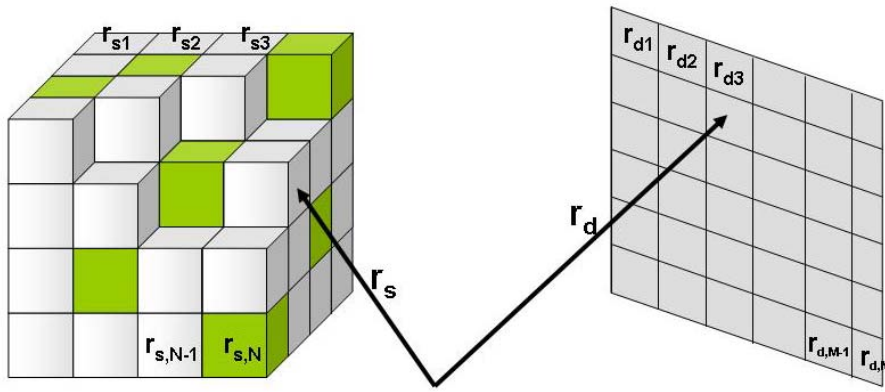


**Figure 4.1:** the correlation between source voxels and detector points

## 4.2 Weight Matrix

As it was stated before, in order to obtain the tomographic image we discretize the subject into  $N$  volume elements, called voxels. In a similar way we discretize also the detector's area into  $M$  detector points. From now on these voxels will be considered as the  $N$  sources of our inverse problem and their signal will be collected by the  $M$  detectors of plane B.

In Figure 4.1 we can see the volume  $V$  created by the  $N$  voxels and the image plane B of the CCD which is consisted of the  $M$  detector points. The fluorescent sources spatial distribution, whose reconstruction is the aim of the tomographic problem, is defined as  $f(\mathbf{r})$ . We will assume that in each voxel the function  $f(\mathbf{r})$  is constant and that the center of each voxel will be given by  $\mathbf{r}_j$ . Let  $f_j = f(\mathbf{r}_j)$  denote this constant value in the  $j$ th voxel.

The contribution of each voxel is correlated with the measurement of each detector point through the following relation:

$$\sum_{j=1}^N w_{ij} f_j = p_i \quad i = 1, 2, \dots, M \quad (4.18)$$

where  $w_{ij}$  is the weighting factor that represents the contribution of the  $j$ th voxel to the  $i$ th detector point. If we write Eq. (4.4) in an expanded form we get the following set of linear equations:

$$\begin{aligned} w_{11}f_1 + w_{12}f_2 + \dots + w_{1N}f_N &= p_1 \\ w_{21}f_1 + w_{22}f_2 + \dots + w_{2N}f_N &= p_2 \\ \vdots & \\ w_{M1}f_1 + w_{M2}f_2 + \dots + w_{MN}f_N &= p_M \end{aligned} \quad (4.19)$$

This system of equations can be written in a form of matrices:

$$\begin{bmatrix} p_1 \\ p_2 \\ \vdots \\ p_M \end{bmatrix} = \begin{bmatrix} w_{11} & w_{12} & w_{13} & \dots & w_{1N} \\ w_{21} & w_{22} & w_{23} & \dots & w_{2N} \\ \vdots & \vdots & \vdots & & \vdots \\ w_{M1} & w_{M2} & w_{M3} & \dots & w_{MN} \end{bmatrix} \times \begin{bmatrix} f_1 \\ f_2 \\ \vdots \\ f_N \end{bmatrix} \quad (4.20)$$

which can also be written as  $P_{M \times 1} = W_{M \times N} \times F_{N \times 1}$ . The P matrix represents the signal that reaches the detector; the F matrix expresses the fluorescent sources distribution in each point  $r$  inside the volume  $V$ . Finally, the W matrix is called *weight matrix*, and represents the contribution of each voxel to the signal measured from each detector point. A method to solve the above system of linear equations is to invert the weight matrix; this task comprises the inverse problem. We will elaborate on the inversion of weight matrix later in this thesis, in our attempt to unmix signals of different spectral regions.

### 4.3 The Algebraic Reconstruction Technique (ART)

In the analysis presented above, we presented how the problem of extracting the fluorescent distribution can be transformed into a matrix inversion problem[24]. Matrix inversion can be performed in different ways depending merely on the size of the matrix. Simple matrices can be inverted through known mathematical formulas. In the case of matrices of large dimensions most of which are correlated, algebraic methods are implemented. The Algebraic Reconstruction Technique (ART) is an

iterative technique, based on the method of projections and it is presented in this section.

In the general case of a problem with N variables, the measured by the CCD signal is described by a system of N equations. This system gives N degrees of freedom to the fluorescence source distribution pattern. Therefore, our imaging target represented by  $(f_1, f_2, \dots, f_N)$ , may be considered to be a single point in a N-dimensional space. In this space each of the above equations represents a hyperplane. When a unique solution to these equations exists, the intersection of all these hyperplanes is a single point giving that solution.

This concept is further illustrated in Figure 4.2 where for the purpose of display, we have considered a simpler case of only two variables  $f_1$  and  $f_2$ , satisfying the following equations:

$$\begin{aligned} w_{11}f_1 + w_{12}f_2 &= p_1 \\ w_{21}f_1 + w_{22}f_2 &= p_2 \end{aligned} \quad (4.21)$$

Each equation represents a line in the two dimensional space  $(f_1, f_2)$ . The solution to the system of Eq. (4.7) is given at the intersection of the two lines.

The computational procedure for locating the solution in Figure 4.2 consists of first starting with an initial guess  $(f_1^0, f_2^0)$ , projecting this initial guess on the first line, reprojecting the resulting point on the second line, and then projecting back onto the first line and so forth, until the intersection point is reached. Projection from the one line to the other and back comprises one iteration. If a unique solution exists, the iterations will always converge to that point.

The extraction of a tomographic image with the inverse method proposed in this section is an ill posed problem and this means that there is not a unique solution. As a result, many different configurations of the fluorophores may give the same results. Below we present an analysis for the case of a well defined problem in order to demonstrate the role of the numbers M and N.

After we have introduced Figure 4.1 which describes the way that the set of equations is formed and Figure 4.2 which refers to the way that we reach at the solutions of our problem, we refer again to the general tomographic problem with the system of N equations (N source voxels and M detector points). We can distinguish three cases, depending on the values of N and M, in order to solve the problem. When

$M=N$  the system has a unique solution and we have a well defined problem. A not uncommon situation in image reconstruction is when we have  $M > N$ . This problem is called overdetermined. This means that there are more equations than unknowns and as a result the system cannot give a unique solution. In the case that  $M < N$ , we say that our problem is underdetermined. The number of the equations is less than the number of the unknowns, and the problem can have infinite number of solutions.

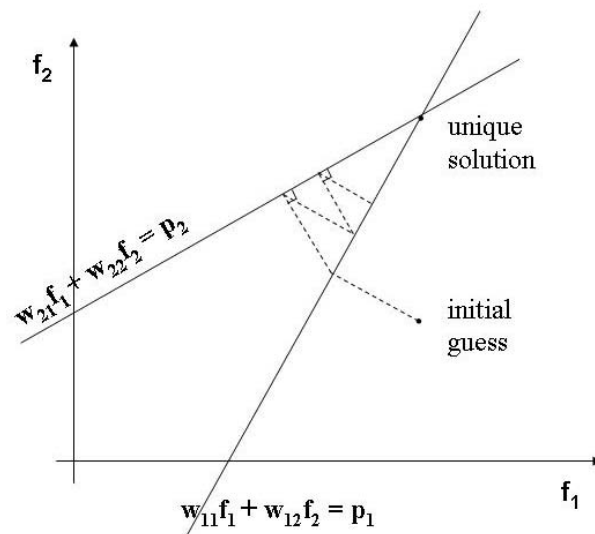


**Figure 4.2:** the initial guess, the projected points onto the two equations and the unique solution of 2-D well defined problem

# Chapter 5

## Materials and methods

In this chapter, an overview of the equipment implemented and the subjects measured for the purposes of this work is outlined. The need of standardisation and calibration of the Fluorescence Molecular Tomography system requires the use of samples that satisfy certain conditions. These samples are tissue-simulating objects that mimic the properties of human or animal tissues. These so-called “phantoms” apart from the known properties must also result from an easy preparation procedure. This is the reason why tissue-like phantoms were preferred for these experiments. The preparation procedure as well as a short reference to the usage of phantoms in the literature will be presented in the following lines. Furthermore the Fluorescence Molecular Tomography system and the experimental geometries employed are also thoroughly discussed in this chapter.

Tissue-like phantoms have been widely used for validating models of light propagation. Moreover the development of all diagnostic imaging systems and most physical therapeutic interventions has required the use of such phantoms. Phantoms are used for many purposes, including: optimizing signal to noise ratio in existing systems, performing routine quality control, and comparing performance between systems. In the case of Fluorescence Molecular Tomography the use of phantoms was imposed in order to control and optimize/calibrate the sensitivity and the resolution of our FMT system.

## 5.1 Tissue- like phantoms

Tissue-like phantoms are playing a very critical role in the fields of optical spectroscopy and imaging. Phantoms that model the transport of visible and infrared light in biological tissue are widely used in order to evaluate techniques, to calibrate equipment and to optimize procedures. Consequently, it is of great importance for the phantoms to mimic the properties of biological tissue and have similar behaviour when illuminated by laser light.

An optical phantom is developed by mixing the correct proportions of the scattering and absorbing media in the solvent, so that the resulting suspension has the desired intrinsic optical properties of the simulated tissue. These optical properties include the absorption coefficient,  $\mu_a$ , the scattering coefficient,  $\mu_s$ , the anisotropy factor,  $g$ , and the index of refraction  $n$ .

Phantoms consist of a scattering medium, an absorbing medium, a solvent, fluorophores, and in case of a solid phantom, a matrix material. In choosing the most useful phantom materials and design, the geometrical properties like thickness, heterogeneities, the mould shape, and possible machining constraints, are important issues that have to be considered. The biological compatibility in terms of biochemical action or inclusion of biologically relevant fluorophores is critical as well. This requires the use of biologically compatible structures such as agar, gelatine, or collagen matrixes that allow easy inclusion of cellular constituents such as blood or lipid emulsions as absorber and scatterer, respectively[25]

In most tissue phantoms, the choice of a scattering agent is separate from the choice of matrix composition, as the volume fraction of the scattering material is typically around the 5% of the total or even less. In the literature we come across three main choices: lipid microparticles, polymer microparticles, and white metal oxide powders. In our measurements we have used Intralipid-20% and titanium dioxide ( $\text{TiO}_2$ ) as scatterers. Intralipid is a lipid emulsion that contains soybean oil, egg phospholipids and glycerol and is also used as an intravenously administered nutrient in hospitals. It is a polydisperse solution of particles with an average diameter of  $\sim 0.4 \mu\text{m}$ , but a relatively wide range of sizes (i.e. from  $\sim 0.1 \mu\text{m}$  to  $\sim 1.1 \mu\text{m}$ ). The number 20% refers to the scattering microparticles concentration in the Intralipid solution. The soybean oil microparticles determine the light diffusion inside the

phantoms. The phospholipids and glycerol are responsible for the homogeneous distribution of the scattering particles in the solution. The benefit of lipid microparticles emulsions, like Intralipid, is that they are biological similar to what is thought to cause scattering in tissue, that is, the bilipid membrane of cells. The drawback, though, of using such fat emulsions is that they slightly fluoresce when excited by wavelengths of the visual spectrum. The study of autofluorescence removal that is presented later in this thesis was based on this fact.

**Table 1:** constituents of Intralipid-20%

	soybean oil	egg phospholipids	glycerol	water
Intralipid-20%	200g	12g	22g	1000 ml

On the other hand, titanium dioxide ( $\text{TiO}_2$ ) is the main pigment in white paint and white plastics, due to their high scattering coefficients, and they can be obtained in well-controlled spherical formulations. The main disadvantage of  $\text{TiO}_2$ , apart from being anything but a biological material, is that it resides in suspension in most media, and settles when not stirred. Of course this is not a problem in resin or agar phantoms once they are set, but it is an issue for aqueous solutions.

As far as the absorption of the phantoms is concerned, either organic like whole blood and haemoglobin or inorganic materials such as ink and other molecular absorbing dyes can be added to achieve the desired value of absorption coefficient for each phantom. In our experiments we have used ink as absorber and the  $\mu_a$  of our phantoms varied between 0.2 and 1.4  $\text{cm}^{-1}$  depending on the experiment. For fluorescence imaging studies a tissue phantom should also host a known concentration of fluorophore with well-known spectral properties.

A liquid phantom is very easy to prepare; however, it cannot be used to make samples of realistic complexity. Solid phantom samples have been made using either transparent hosts, like agar, polymers, or gelatine; or using inherently light-scattering material such as wax. Polymer-based phantoms have been reported to crack if they are too large or to shrink during polymerization, which limits their applicability. Gels contain a solvent that evaporates, changing thus the dimensions and the optical properties of the samples within a short period.

An ideal phantom, in order to simulate tissue fluorescence, should provide the experimentalist with independent control of its optical properties[26]. It is important

to note that, while both fluorophores and absorbers contribute to the absorption coefficient, it is desirable that both scatterer and host material are non absorbing and nonfluorescent. If this is achieved – by choosing the appropriate materials – the optical properties of the phantom samples can be easier controlled and determined.

A realistic tissue phantom should satisfy the following requirements [27]

- It should model the geometry and optical parameters of the physiological structures that are relevant for the transport of light.
- All components must be compatible with each other regarding chemical stability and spectroscopic properties.
- The relevant parameters of radiation transport must be both reproducible and predictable from the sample composition.
- The physical parameters of the phantom sample should be temporarily stable (evaporation, diffusion, aging) and independent of environmental influence.
- The phantom should allow the construction of inhomogeneous samples by stacking phantom slabs or by elaborate moulding techniques

and the most important

- The sample preparation should be simple, quick and safe.

### **5.1.1 Preparation of phantoms**

For our experiments we have used both solid and liquid phantoms. In the following paragraphs the solid phantom preparation procedure is described, according to the literature [28]. For the needs of this thesis water-based phantoms were prepared. The desired optical properties of the phantoms were reached by adding appropriate amounts of absorbing (India ink) and scattering media (Intralipid-20%, TiO<sub>2</sub>) in distilled water.

A highly purified agar powder (A-7049, Sigma, USA) is dissolved in distilled water in the appropriate concentration (1-2%) and heated up to the melting temperature of 95°C. We bring the solution to a boil using a microwave oven until the solution becomes homogeneous. The agar solution alone has negligible absorption and very low turbidity. Therefore, the desired optical properties are achieved by adding the appropriate amounts of Intralipid-20% (Fresenius Kabi, Germany) or TiO<sub>2</sub>, as scattering media, and India ink (Rotring, Germany), as absorbing medium. The

optimal temperature  $T_{\text{mix}}$  for adding Intralipid and ink is rather non-critical in the range between  $80^{\circ}\text{C}$  and  $40^{\circ}\text{C}$ , and we usually work with  $T_{\text{mix}} \approx 60^{\circ}\text{C}$ . While waiting for the solution to cool down it is important to stir it continuously, in order to obtain good uniformity.

At  $40^{\circ}\text{C}$  the solution must be poured into a mould and left there for some minutes to reach a proper hardening and stable optical properties. In our case, where agar concentration was 2% of the solution, 15 minutes were an adequate time period for the mixture to be completely hardened. For the needs of our experiments two kinds of moulds have been used, resulting, thus, to two different shapes of phantoms; cylindrical and planar (slab) phantoms Figure 5.1. The former were Teflon cylinders with a 20mm diameter hollow and 0.5 mm wall thickness, mostly used with the first generation of the FMT experimental setup. The latter were slab phantoms and were the phantoms used for all the measurements presented in this thesis. A  $100\text{mm} \times 80\text{mm} \times 12\text{mm}$  custom-made aluminium frame was used with two transparent  $100\text{mm} \times 80\text{mm}$  plexiglass plates side walls. The plexiglass plates could be later removed so as the laser beam could directly illuminate the agar phantom.

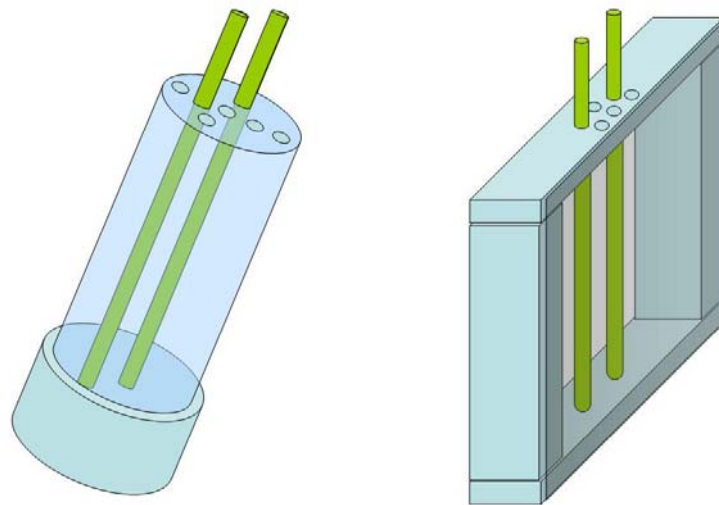


**Figure 5.1:** the cylindrical and the slab phantom moulds

In the case of a liquid phantom the preparation procedure was faster and much easier. The liquid phase of the mixture did not require the addition of agar powder as hardener and, therefore, only mixing of the constituents and stirring for a few minutes were required for the solution to be prepared. The main advantage of liquid phantoms

was that we could prepare many of them right before or even during the experiments. On the other hand, solid phantoms preparation required about 60 minutes, making thus the experimental procedure longer lasting.

In order to induce fluorescent concentration in specific positions inside the phantoms borosilicate micro capillary tubes (Drummond Scientific,US) with an outer diameter of 1.8mm and an inner of 1.2 mm were embedded in the phantom material. As fluorophores we have used carboxyfluorescein succinimidyl ester (CFSE) solved in 1×phosphate-buffered saline solution with pH of 12. CFSE exhibits a fluorescence peak at 517nm and is widely used for simulating the emission of the Green Fluorescence Protein (GFP) molecule. We also used Atto-590 (Atto-Tec, Germany) which is a new fluorescent label belonging to the class of Rhodamine dyes. It exhibits absorption peak at 594 nm and fluorescence peak at 624 nm.

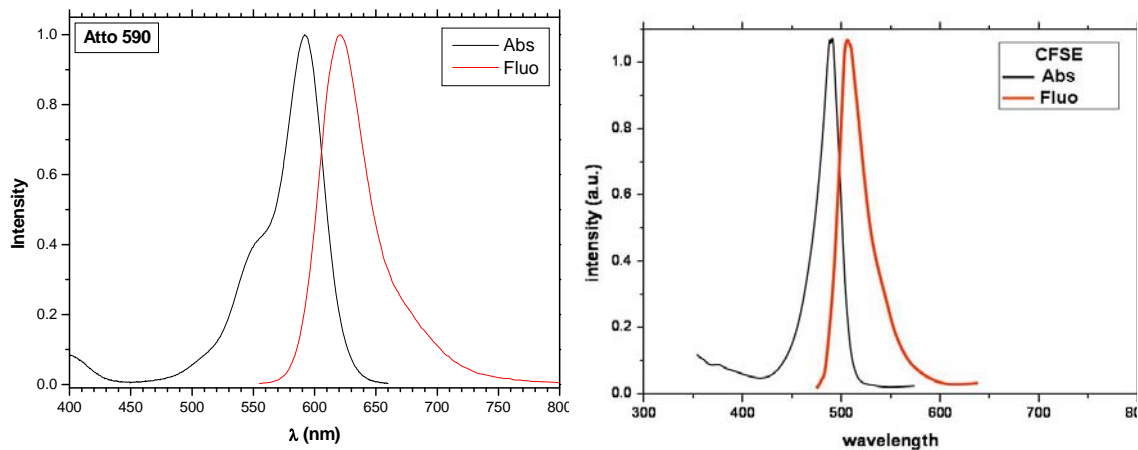


**Figure 5.2:** absorption and emission spectra of (a) Atto590 and (b) CFSE

### 5.1.2 Mice

Transgenic control mice were used for the needs of some experiments. That is mice that are not engineered to have a functional expression of a specific protein (they are usually used for calibrating measurements). The few mice used in our experiments had a black fur covering their body. When performing optical measurements, the black fur causes attenuation on both the illumination light entering the body and on the light emerging from the body. For this reason, shaving of the mouse fur is necessary, in order to expose the skin at the region of interest. In order to immobilize the living samples during the experiments an Isoflurane vaporizer was used.



wavelength by placing laser line filters in front of the laser source. For the experiments presented here we have used the three main emission lines of the laser. The experiments were carried out inside a 5mm thick custom-made aluminium black anodized imaging box for ambient light isolation of the setup (ii) (shown transparent in Fig. 5.1 for illustration purposes).

The laser light is directed to the sample by a group of stable, moving and flip mount mirrors. The laser beam is guided inside the imaging box with the aid of two flip mount mirrors (iii). Inside the box there is another pair of mirrors (iv) that lead the beam into a laser scanning device (Scancube 7, Scanlab) (v) which incorporates a system of mirrors mounted on miniaturized galvanometer motors Figure 5.4. The mirrors are being controlled by the software and therefore the laser beam is guided in a two directions movement. The system described above is used to perform the scanning on the imaging sample. The laser light is guided to the sample with the use of two large rectangular mirrors (first surface mirrors, 4-6 Wave, 73mm×116mm, Edmund Optics) (vi). The one of them is mounted permanently on the ceiling of the box, while the other lies on the optical table and moves along a rail between two fixed positions, determining thus the geometry of the scanning. For measurements in the reflection geometry the bottom mirror is moved forth, to position 1, Figure 5.6, so that the laser beam, after being reflected by the bottom mirror first and by the top mirror right afterwards, illuminates the sample from the side of the camera. For measurements in transmission geometry the bottom mirror is moved to position 2, so that the laser light illuminates the sample from the bottom side.

The sample is placed on a transparent glass plate with an anti-reflection coating (vii) (Glassplate, High AR coated 96-99% (400-700nm), 5"×7", Edmund

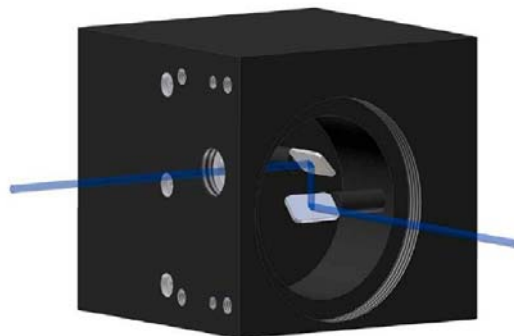


**Figure 5.4:** the scanning head with the motorized mirrors and the route of the laser beam

Optics). The glass plate is mounted on a platform (*viii*) that is placed on an X-Y translation stage. The X-Y movement aligns the subject in respect with the camera axis. Depending on the desired resolution of each measurement the distance of the sample from the camera (height of the sample) can be modified by placing the glass plate in one of the four different fixed positions along the Z axis. The plate is mounted to the stages with a simple custom-made clip system so that it can be easily removed and put back in the setup for the repetition of the measurements. The signal acquisition was provided by a thermoelectrically cooled 16bit CCD camera cooled down to  $-70^{\circ}\text{C}$ , with a chip size of  $1024 \times 1024$  pixels (*ix*) (Andor Corp., DV434, Belfast, Northern Ireland). The CCD camera is equipped with a SIGMA 50mm  $f/2.8$  objective (Sigma Corporation, Tokyo, Japan) (*x*) which was focused on the sample's surface. The CCD camera is mounted on the upper plate of the imaging box. Data acquisition was performed on a 3.0 GHz PC with 512 MB RAM (*xi*). For spectral data acquisition of our imaging samples we have used a custom-made concave grating spectrograph (*xiv*). On the spectrograph we have attached a CCD camera similar to the one described above.

In the case of in vivo imaging the samples have to be anaesthetized first. For this reason a TeC-3 Isoflurane vaporizer (*xii*) (Lumic International, 21220 Baltimore MD) is used. The output of the vaporizer can be directed either to an anaesthetization

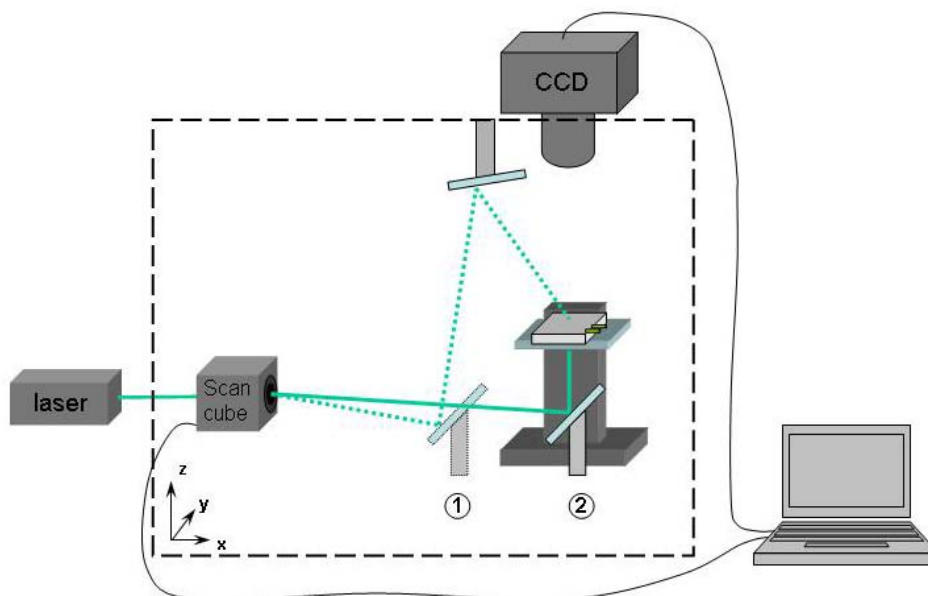


**Figure 5.5:** the two experimental geometries. Reflection measurements when the bottom mirror is in position 1; Transmission measurements when the bottom mirror is in position 2, under the sample

chamber (*xiii*) or into the imaging box, on the glass plate, to a custom-made mask that adjusts on the living sample.

In order to select between the excitation and the fluorescence signal detection, anti reflection coated emission band pass interference filters (55mm diameter) are used (Chroma Technology Corp., Bellows Falls, VT 05101, US). For the excitation of the CFSE we applied a 488 nm bandpass filter (3nm bandwidth, 25mm diameter, 488FS03-25, Andover, USA) and a 458 nm bandpass filter (1.7nm bandwidth, 12.5 mm diameter, LL01-442-12.5, Laser 2000, UK). For the recording of the CFSE emission a 40nm bandwidth filter (centred at 520nm) was used. For the excitation signal detection we used a 55 mm diameter, 60 nm bandwidth filter (centred at 480nm) in front of the camera.

The basic characteristics of the first generation's FMT setup that differentiated it from the setup just described above were, firstly, the samples position; instead of lying on the glass plate it was hanging from a rotation stage in front of the camera, so there was also the possibility of the rotation of the sample in small angles. Secondly, the laser scanning was being performed by translational stages instead of the galvanometer motor-controlled mirrors. Finally the laser light was directed to the sample by an optic fiber instead of the group of mirrors that is today used. Another important part of the older setup is the surface reconstruction process through which we could reconstruct the surface and, thus, the volume of the imaging sample.

All the components of the setup described above are controlled through a program made in Labview environment. This program gives us the ability to control the simultaneous operation of the setup components. As a matter of fact, we define the parameters of each experiment, i.e. the laser beam movement (through the scanning head), the exposure time of each measurement, and the temperature of the camera chip. The data acquired is stored in the form of a stack of two dimensional images. These data are later processed with a custom-made Labview code in order to achieve the three dimensional reconstruction of the fluorescent region inside the sample's volume.

# Chapter 6

## Experiments & results

### 6.1 Experimental procedure

In the previous chapter, the experimental setup and the imaging samples preparation procedure were described. In this chapter the procedure followed for performing our experiments will be outlined.

#### 6.1.1 Data collection

After the sample has been prepared, it is placed on the imaging platform of the FMT system, in front of the CCD camera. Depending on the sample and on the region that we want to image, we choose the geometry of the measurement, the way the sample is placed on the platform and the height of the platform, that is the distance from the camera's objective lens. The selection between reflection and transmission geometry is usually made regarding to the position of the sample volume that we want to image. In the case of a phantom this does not make any difference due to the phantom's simple structure. On the contrary, when the sample is a mouse the geometry selection depends on whether the volume that we want to image is placed superficially or deeper in the mouse body. Moreover, the required resolution and precision of our measurements determine the distance from the camera that the sample is placed. In most of the experiments presented in this thesis both reflection and transmission geometries were used in order to compare the results and screen their differences.

Once the sample is fixed we set the parameters of each experiment on the software developed in LabView™ environment. We set the sources (illumination points) and the exposure time for each measurement. The arrangement of the sources is chosen according to the shape and the size of the sample volume that we want to image, while the number of sources is determined by the resolution requirements of each experiment and, of course, restrained by the duration of measurements. The duration of an experiment is an important issue especially in the case of in vivo experiments, where the animal is kept under anaesthesia.

After we have defined the source pattern, the emission and excitation signals are acquired using the respective filters. For the case of CFSE we illuminate with the 488nm line of the Ar<sup>+</sup> laser. The fluorescence and the excitation intensities are collected by using two bandpass emission filters in front of the camera, selecting, thus, the regions of wavelength detected each time. In Figure 6.1(a)-(c) the filters' profiles as well as the absorption and emission spectra of CFSE are presented. Each figure refers to a separate measurement taken during an FMT experiment.

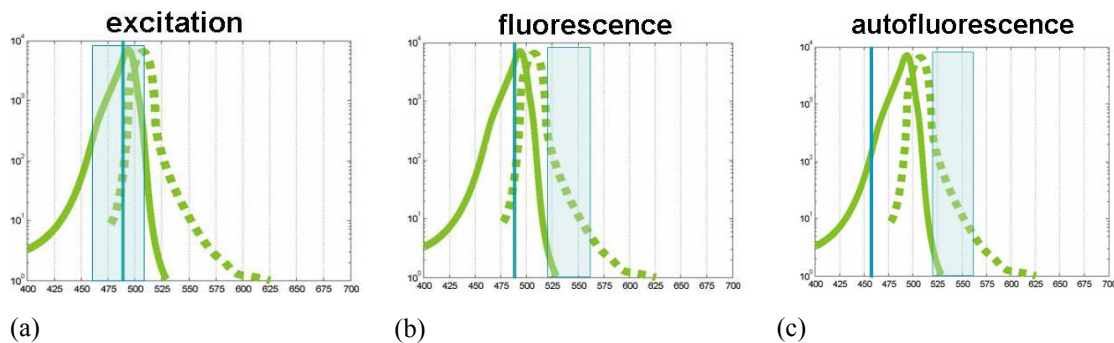


**Figure 6.1:** three measurements taken with the combination of laser lines and filter profiles: excitation, fluorescence and autofluorescence measurements respectively

Figure 6.1(c) presents the autofluorescence measurement obtained while exciting the fluorophore with the 458nm laser line. This measurement is taken in order to acquire an expression for the surrounding medium's emission intensity at the fluorophore's fluorescence region ( $540 \pm 20\text{nm}$ ). The autofluorescence measurements aim at the background fluorescence of tissue, which is particularly high in the visible region of the light spectrum, reducing, thus, the detection sensitivity and the imaging performance of the FMT system. The main idea behind this measurement is to illuminate the sample at a wavelength far from the excitation peak of CFSE so as to mostly record the tissue autofluorescence. The autofluorescence measurement is an

additional measurement and it is not inserted into the tomographic calculations. However it is used in an unmixing algorithm that also uses spectral data of the sample's constituents in order to achieve the autofluorescence removal, as it will be thoroughly described in following paragraphs.

The camera acquires the data sequentially as a series of 2-dimensional images, one for each illumination source. As a result of this, every measurement is being recorded as a stack of 2-dimensional images. Consequently, each one of the excitation and fluorescence measurements will be recorded in the form of a 3-dimensional matrix resulting from the product  $N_x \times N_y \times N_s$ ; where  $N_x$  and  $N_y$  are the number of pixels of the CCD chip in x and y axes respectively (1024×1024 chip turned into a 512×512 due to 2×2 binning applied to the camera), and  $N_s$  is the number of the sources arranged.

### 6.1.2 Data processing

Once the experiment has finished and we have taken the corresponding measurements we process the data so as to extract the tomographic image. The processing of the data is being performed through software developed in LabView™ environment.

In order to progress with the processing of the data we set the input parameters on the software. First of all we set the detectors pattern. This procedure is similar to the sources' pattern arrangement procedure. In our case that we illuminate a specific region of our sample, there is no need to cover the whole surface of the sample with detectors. The detectors pattern is usually set in a region a little wider than the region that the source pattern covers. Each pixel of the camera can be a single detector, resulting in an array of thousands of single detectors. Combining the signal of neighbouring pixels results into an even more effective detector. Detectors may also overlap although in all the experiments presented in this thesis they were chosen to be separate. In the experiments presented here a typical value of a single detector's diameter was 0.1 cm. The detectors are usually arranged in rectangular patterns, covering an area 10mm×10mm.

Other parameters that are set on the software are the optical properties of the sample, the geometrical properties as well as the size and the number of the Mesh points. As mentioned in the theory earlier, in order to obtain the tomographic image we discretize the subject into volume elements, called voxels. These voxels form the

mesh volume. Their number can be determined separately in each axis, giving thus the required precision and sensitivity to our measurements.

The Normalized Born image, as analyzed in Chapter 4, is calculated by dividing the fluorescence measurement with the excitation measurement. After that, the normalized measurements are inverted with the Algebraic Reconstruction Technique (ART) in order to create a map of the spatial distribution of the fluorescent concentration inside the reconstructed volume of our sample. Typical values of the number of iterations vary between 100-1000 depending mostly on the experiment. Moreover the inversion times were in the order of 5-10 minutes on a 2 GHz Processor with 1GB RAM with mesh values ranging between 500 and 5000 voxels.

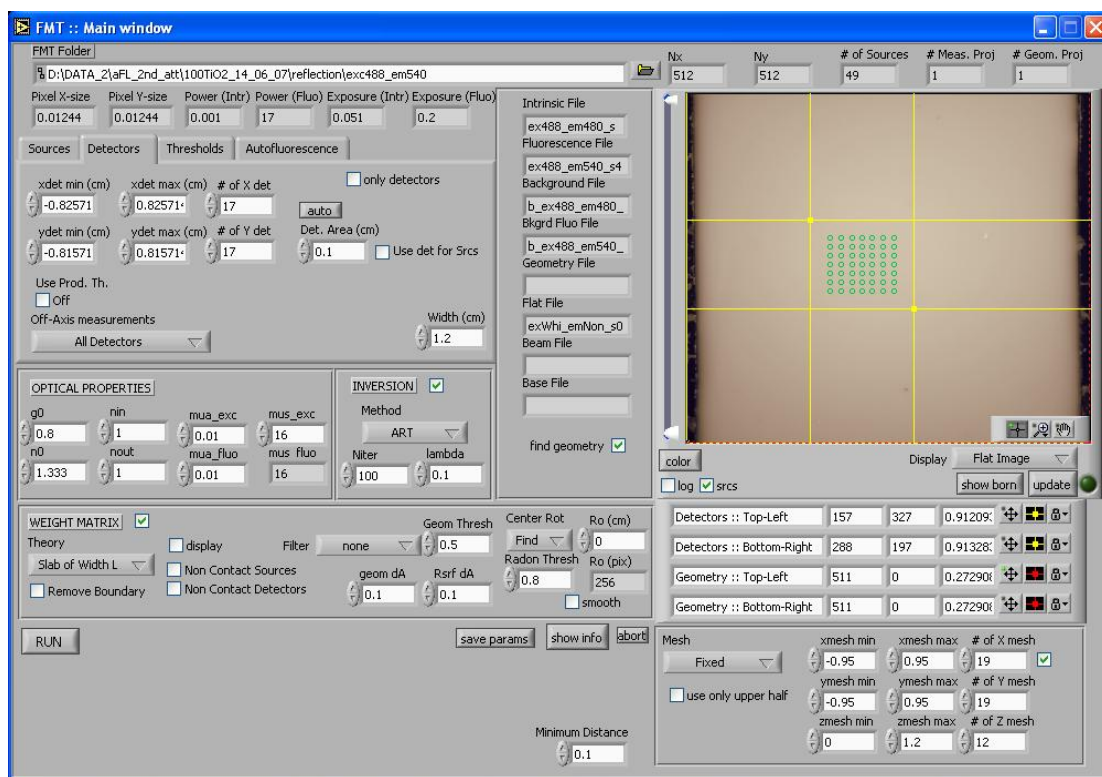


**Figure 6.2:** the reconstructions were extracted through a code developed in Labview software, where we were inserting the experimental parameters

## 6.2 Experiments and Results

A large number of experiments were performed for the needs of this work. In the most of them the imaging samples were tissue-like phantoms, solid or liquid, that were containing glass tubes filled with fluorophores, CFSE or Atto590. Experiments with mice were also performed in some cases. The fluorescent concentrations were later reconstructed by applying the methodology described in the previous chapters.

In the first section, we present experiments driven by the need of calibrating the setup. In that direction, glass tubes, filled with different concentrations of the same fluorophore, are immersed in the phantoms performing, thus, a quantification experiment. The aim is to demonstrate the capacity of the FMT setup to quantify the different fluorescent signals inside the scattering media. Next we present measurements on phantoms containing two tubes filled with CFSE, placed each time in different distances from each other. The determination of the closest distance that two light emitting volume elements can be placed inside a turbid medium in order to be imaged and reconstructed as two single objects is always an issue in imaging systems. Therefore, an attempt to perform resolution experiments is also presented in this thesis.

Finally, we present a study on unmixing signal from different fluorescent probes based on a linear unmixing algorithm applied to spectral imaging. Results of two-colour imaging are presented, when the algorithm is applied to separate fluorescence activity originating from phantoms and mice, containing two different fluorophores with well separated emission spectra, namely CFSE and Atto-590. Besides a basic part of this study consists the attempt that we have made to remove the autofluorescence signal of our imaging samples. Instead of having two fluorophores, we have used CFSE and a slightly fluorescing material (Intralipid) trying therefore to unmix their emission signals.

### 6.2.1 Quantification

In this section, the results of the quantification experiments are presented; performed with our system on both cylindrical and slab phantoms. In the first part, measurements were performed on a hollow Teflon cylinder, 20mm in diameter with 0.5mm wall thickness, filled with an agarous solution. The resulting solid phantom had a reduced scattering

coefficient  $\mu'_s = 16\text{cm}^{-1}$  and an absorption coefficient  $\mu_a = 1.4\text{cm}^{-1}$ . The capillary tubes were filled with different concentrations of CFSE (1  $\mu\text{Mol}$ , 50  $\mu\text{Mol}$ , 100  $\mu\text{Mol}$ ) and embedded in the phantom at a center to center distance from the capillary to the Teflon cylinder of 5mm. As the experiment was performed with the 1<sup>st</sup> generation FMT setup, the phantoms were rotating in small angles. In this specific experiment we had four projections at 0, 10, 20, and 30 degrees with respect to the incident sample position where the tube was in the closest position to the camera. The  $3 \times 3$  sources pattern adopted was spanned over an area of  $13.4\text{mm} \times 8.0\text{mm}$  on the surface of the phantom, while the  $18 \times 12$  detectors grid was covering an area of  $17.0\text{mm} \times 11.8\text{mm}$ . In order to reconstruct the phantoms we used 14700 mesh points to discretize their volume.

The reconstructions' results are shown in Fig. 6.3. Figure 6.3a presents the 3D reconstructed surface of an agarous phantom with reconstructed fluorescence for the reflection mode. As can be seen in the figure, both the radius of the cylinder and the position of the capillary tube containing CFSE are retrieved with an accuracy of approximately 5% (note that the center of rotation is not necessarily placed on the axes origin). An axial section of the phantom is shown in the inset of Fig. 6.3.b.

The results for the quantification are shown in the graph of Fig 6.3.b. The

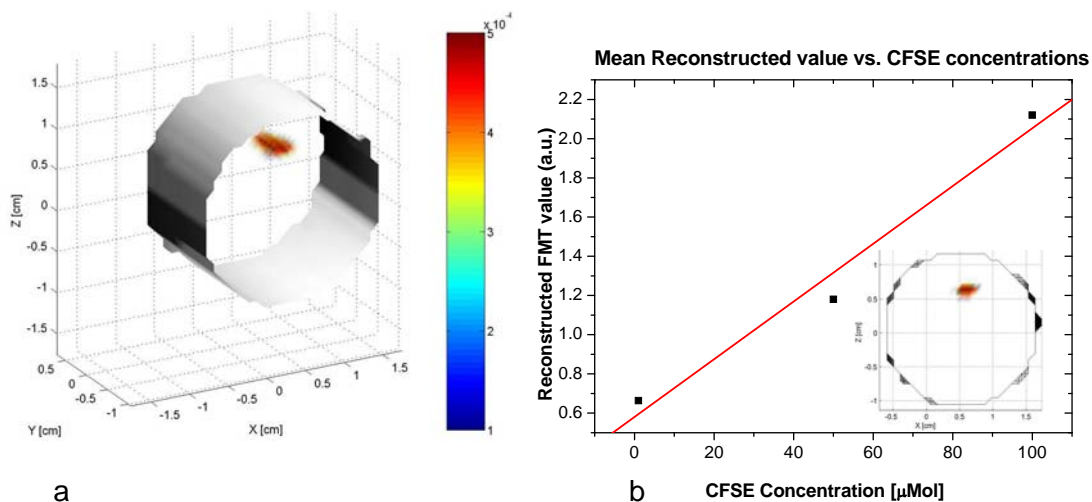


**Figure 6.3:** **a**, Three-dimensional reconstructed surface of an agarous phantom with reconstructed fluorescence using a 50  $\mu\text{mol}$  concentration of CFSE. The microcapillary was placed in a center-to-center distance of 5 mm with respect to the center of the phantom, **b**, reconstructed mean fluorescence intensity values achieved with the FMT system versus CFSE concentration in the microcapillary tube of the agarous phantom (1, 50, and 100 $\mu\text{mol}$ ). (Inset shows cross section of the reconstructed fluorescence according to the values given in a.)

reconstructed mean fluorescence intensity values vs. the CFSE concentration in the tubes are presented. As it can be seen, there is a good linearity between the fluorescent signal and calculated values by the FMT software.

However, in the experiments presented here we have not used the cylinder phantoms but we have used the slab phantoms instead. Moreover in the case of the quantification experiments, liquid phantoms were prepared, as agar was not added as a hardener to the solutions. The advantage of a liquid phantom is that less preparation time is demanded for the preparation. For these experiments both CFSE and Atto-590

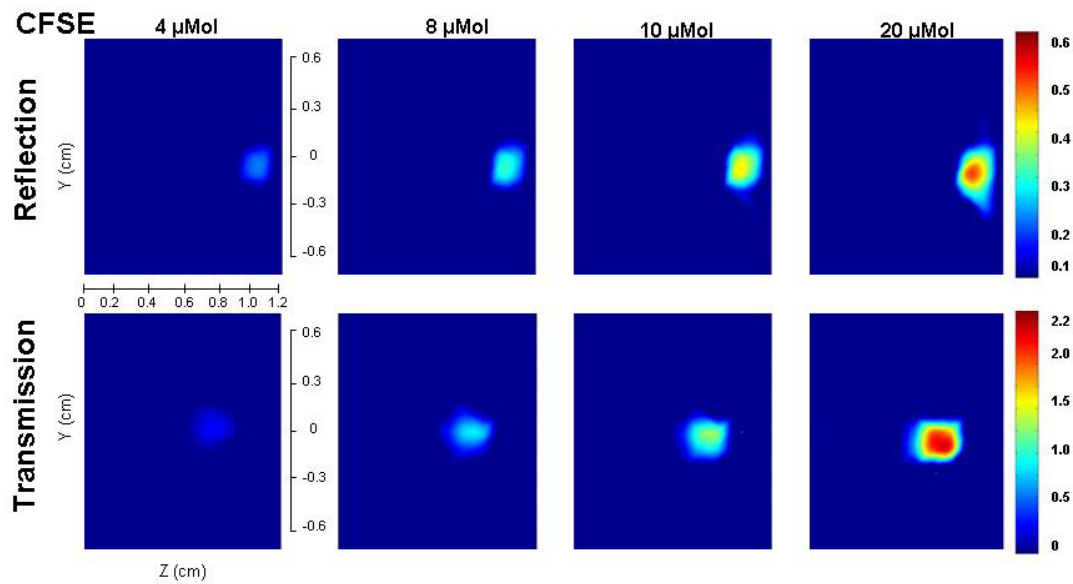


**Figure 6.4:** FMT reconstructions of the different concentrations of CFSE immersed inside the slab phantom in 3mm depth, in Reflection and Transmission geometry, after 100 iterations

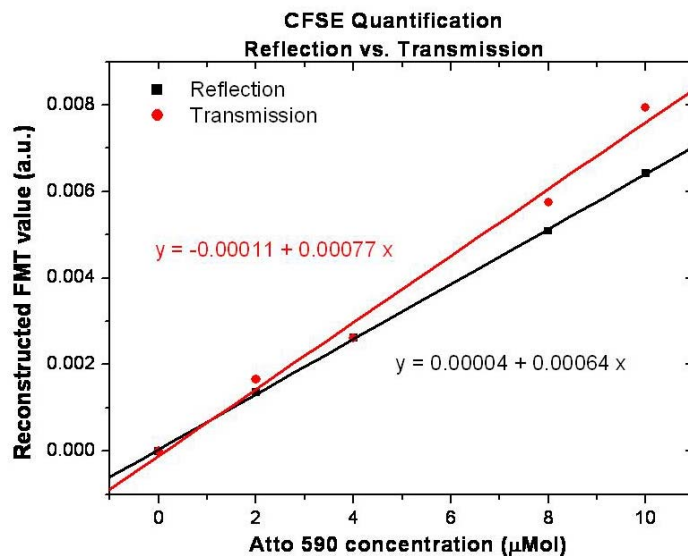


**Figure 6.5:** the linear relation between CFSE concentration and the reconstructed values, in Reflection and Transmission geometry were used. In each phantom one capillary tube filled with the fluorophore was

immersed at the depth of 3mm under the surface that is in front of the camera. After the required measurements were taken, we were sequentially exchanging the measured tube with the rest to be measured. The whole procedure was quite fast and, as a result, the experiments were being completed in a short period of time and the optical properties of the phantoms remained constant. The slab phantom quantification experiments were performed both in Reflection and Transmission .

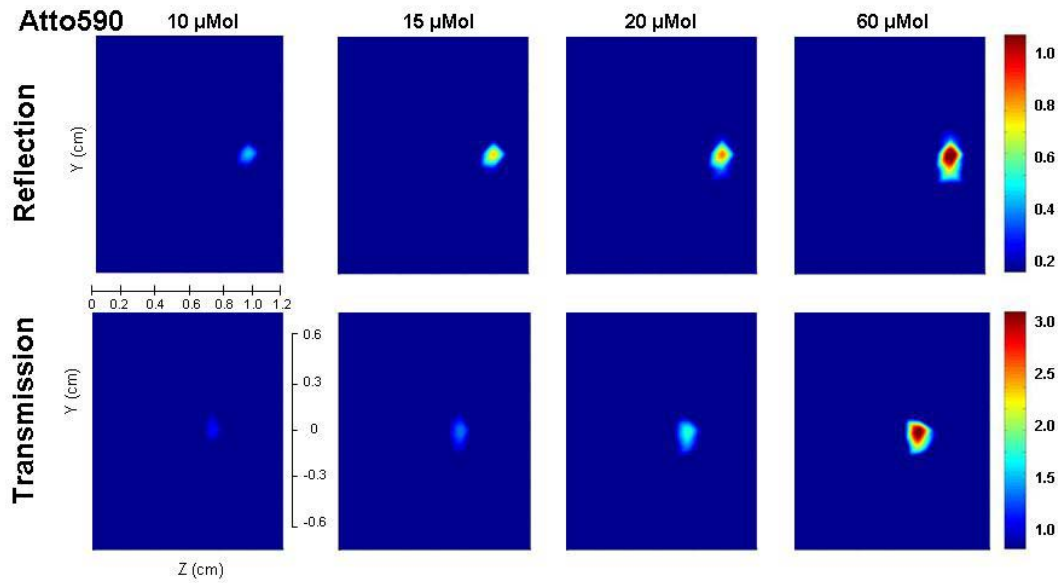


**Figure 6.6:** FMT reconstructions of the different concentrations of Atto590 immersed inside the slab phantom in 3mm depth, in Reflection and Transmission geometry, after 500 iterations

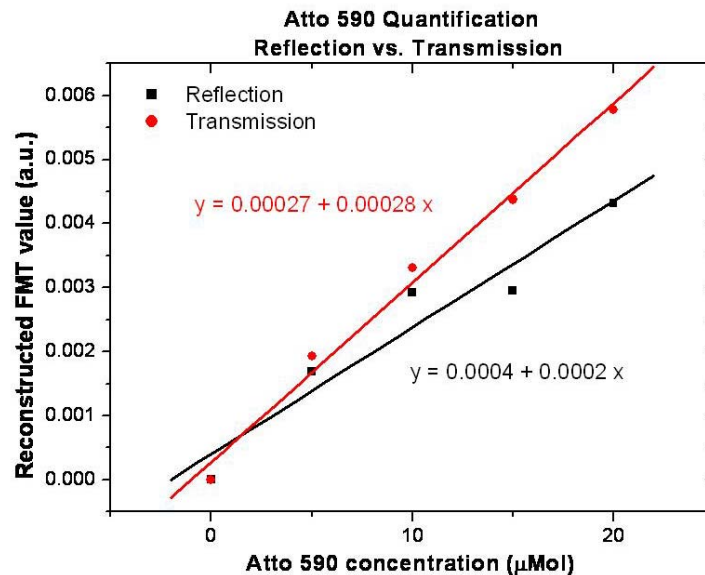


**Figure 6.7:** the linear relation between CFSE concentration and the reconstructed values, in Reflection and Transmission geometry

The phantoms were prepared by pouring the already mixed and stirred solution of the known constituents in the mould that is placed on the platform inside the imaging box of the setup. Before that, we had placed the capillary tube with the desired concentration in the appropriate position. The resulting liquid phantom had a reduced scattering coefficient  $\mu'_s = 16\text{cm}^{-1}$  and an absorption coefficient  $\mu_a = 0.3\text{cm}^{-1}$ . The capillary tubes were filled with different concentrations of CFSE and Atto 590 and were embedded in the phantom in a distance of 3mm from the upper surface. The concentrations of each fluorophore used are the following: for the case of CFSE, we diluted the original stock solution into new solutions with concentration values of 2  $\mu\text{Mol}$ , 4  $\mu\text{Mol}$ , 8  $\mu\text{Mol}$ , 10  $\mu\text{Mol}$ , and 20  $\mu\text{Mol}$ . In the case of Atto 590 the respective concentrations of the new solutions were 5  $\mu\text{Mol}$ , 10  $\mu\text{Mol}$ , 15  $\mu\text{Mol}$ , 20 $\mu\text{Mol}$  and 60  $\mu\text{Mol}$ .

In order to be able to compare and reproduce the outcoming results we have chosen the parameters of all the experiments to be identical, i.e the number of sources and detectors, number of mesh points iterations, etc. Therefore, for performing the illumination of our samples, a  $6 \times 8$  sources pattern was adopted. The sources pattern had dimensions of  $6.2\text{mm} \times 9.0\text{mm}$  and was covering an area of  $55.8\text{mm}^2$ . For the detection area, we used a  $6 \times 14$  detector grid covering an area of  $84\text{mm}^2$ , with a detector size of  $1\text{mm}^2$ . The under study volume of the phantom was discretized in 1260 mesh points and the reconstruction data were extracted after inverting the raw data (measurements) using the Algebraic Reconstruction Technique (ART) for 100 - 500 iterations. Typical times for the mapping of the fluorescence signal were of the order of 2 - 5 minutes on a 2 GHz personal computer with 1 GB RAM.

It must be noted that this type of calibration has to be performed for each fluorophore under study if one intends to represent the measurements in terms of fluorophore concentration.

Also, even though this quantification study has been performed in a homogeneous phantom with optical properties similar to those of mice in the GFP excitation range, we would like to state that thorough studies of the effect of inhomogeneities have been presented recently [23] proving that the normalized approach used here [22] is extremely robust, even in highly heterogeneous media.

## 6.2.2 Resolution experiments

Another important issue in the field of tomography and optical imaging in general, is the resolution of the imaging systems used. Optical resolution describes the ability of a system to detect, distinguish and record physical details of its imaging samples. In our case the term resolution refers to the ability of the FMT system to detect and reconstruct adjacent fluorescing details or inhomogeneities located inside the sample's volume. More specifically, the aim of the experiments presented here is the determination of the minimum distance, that two fluorescing objects can be placed close to each other, at which the FMT setup can distinguish and reconstruct them as two separate objects.

Working on that direction we used liquid slab phantoms with constant optical properties; that is absorption coefficient  $\mu_a = 0.3\text{cm}^{-1}$  and scattering coefficient  $\mu'_s = 16\text{cm}^{-1}$ . The preparation procedure has been thoroughly described in previous sections. As fluorescing objects we used two capillary tubes filled with CFSE solution (diluted in PBS with pH=12) with concentration of 10  $\mu\text{Mol}$ . The tubes had an outer diameter of 1.8mm and an inner diameter of 1.4 mm and were placed at distances of 2.8mm and 0.5mm at the depths of 3mm and 6mm under the surface of the phantom, in front of the CCD camera's objective.

The illumination and the detection patterns were defined in a similar way in order to achieve the easy repetition and comparison of the results. The 2x23 source grid was covering an area of 1.5mm $\times$ 13.2mm. In a similar way, the 4x14 detector grid was covering an 4mm $\times$ 14mm area, with a detector size of 0.5mm<sup>2</sup>. As it can be easily seen, both the illumination and the detection patterns were narrowed in the x axis (along the tubes' axes) and widened along the y axis, normal to the tubes' axes, where more detail was needed.

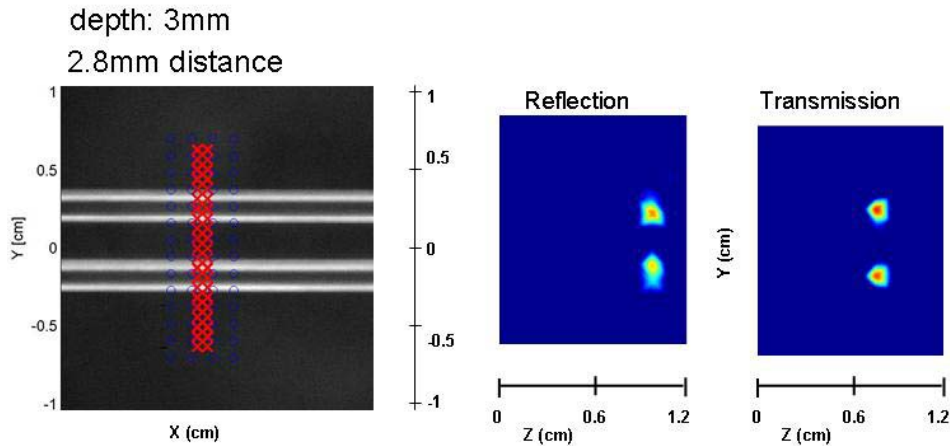


**Figure 6.8:** two dimensional reconstructions of the CFSE ( $10\mu\text{Mol}$ ) tubes placed in 2.8mm distance, in 3mm depth under the surface in front of the camera

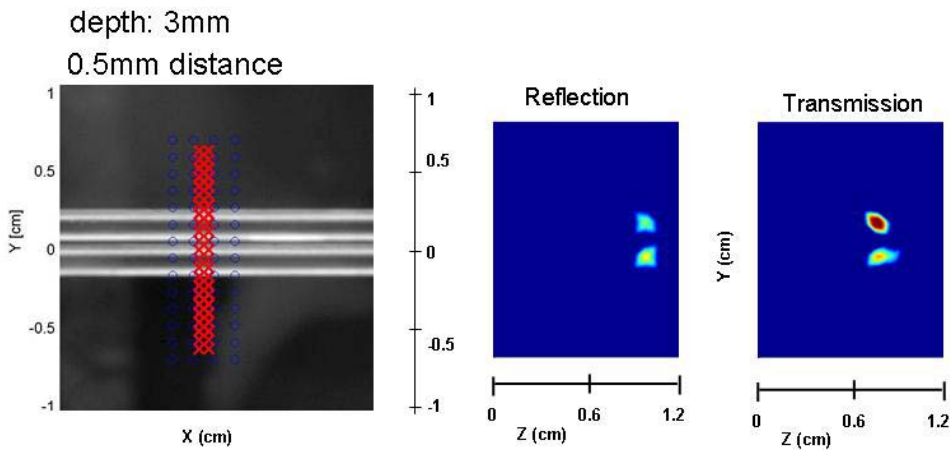


**Figure 6.9:** two dimensional reconstructions of the CFSE ( $10\mu\text{Mol}$ ) tubes placed in 0.5mm distance, in 3mm depth under the surface in front of the camera

For the reconstructions, we chose a small volume with dimensions  $2\text{mm} \times 15\text{mm} \times 1.2\text{mm}$  which was discretized in 540 mesh points. The presented results in Figures 6.8 -6.13 were extracted after inverting the raw data (measurements) using the ART for 10000 iterations. Typical times for the mapping of the fluorescence signal were of the order of 5 minutes on a 2 GHz personal computer with 1 GB RAM.

The results of the resolution experiments are presented in Figures 6.8-6.11. In Fig. 6.8, 6.9 are shown the results from the experiments with the tubes placed in 3mm depth under the surface of the phantom, in front of the CCD. As it is clearly seen, the two tubes are clearly reconstructed at the correct distances, respectively. In Fig 6.9, are shown the results of the closest distance between the two tubes; 0.5mm edge-to-edge distance between the tubes, or else 0.9mm distance from fluorophore to

fluorophore, considering the thickness of the tubes' walls (0.2mm). Both reflection and transmission geometries have succeeded in reconstructing their separating distance. However, we observe that reconstructions resulting from reflection measurements locate the fluorescing volume in a position closer to the surface, compared to the real position and to the transmission respective reconstructions. This, however, is a known characteristic of the theoretical technique used.

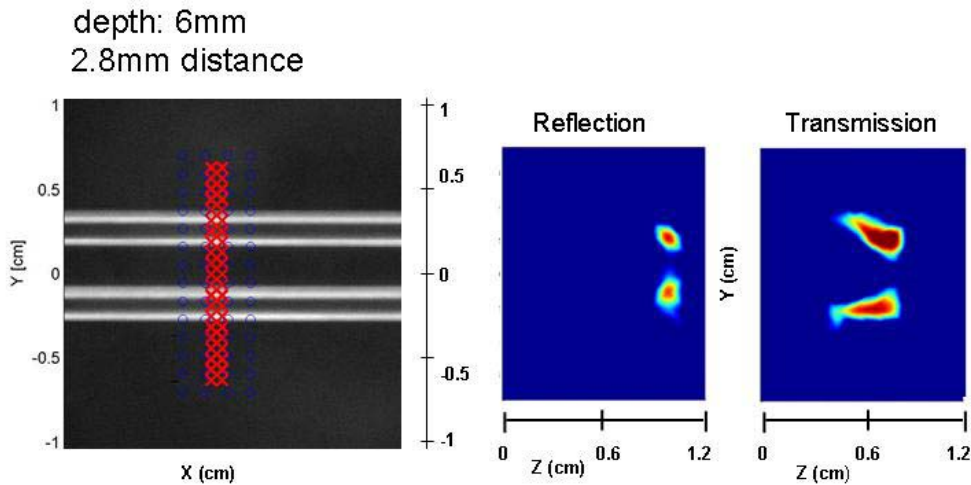


**Figure 6.10:** two dimensional reconstructions of the CFSE ( $10\mu\text{Mol}$ ) tubes placed in 2.8mm distance, in 6mm depth under the surface in front of the camera

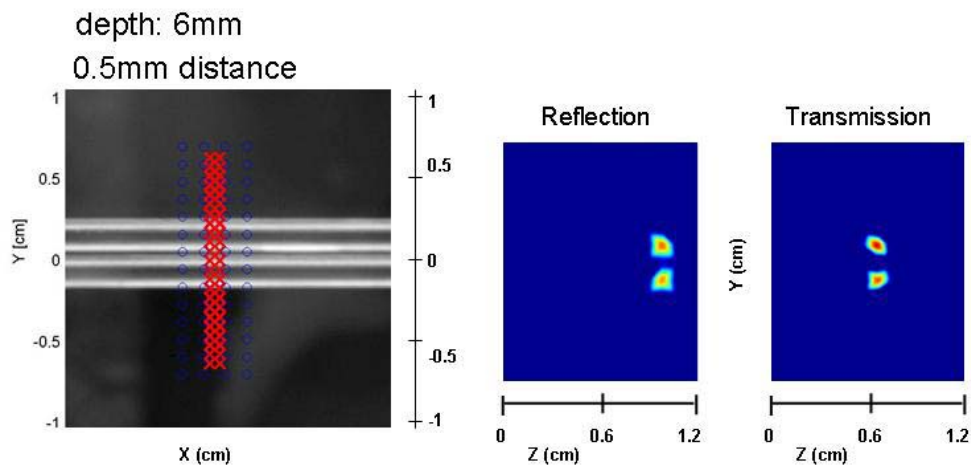


**Figure 6.11:** two dimensional reconstructions of the CFSE ( $10\mu\text{Mol}$ ) tubes placed in 0.5mm distance, in 6mm depth under the surface in front of the camera

In Fig.6.10 -6.11 are shown the results from the experiments with the tubes placed in the middle of the slab phantom at a 6mm depth under the surface of the phantom, in front of the camera. The distance between the tubes is reconstructed precisely. Moreover, the weakness of reflection geometry to locate the tubes in their

correct position is more than obvious. However the transmission results are more correct as compared with the experimental parameters.

Furthermore, another study was performed with the samples described above. We tried to test the capability of the software to reconstruct the correct quantities, while we were varying one input parameter. To that end we performed the reconstructions for different values of the absorption coefficient  $\mu_a$ , for both the experimental geometries, reflection and transmission. The values of the absorption coefficient  $\mu_a$ , were varying in the range of  $0,01 - 0,70 \text{ cm}^{-1}$ , with increment of  $0,1 \text{ cm}^{-1}$ . The results are presented in Figures 6.12, 6.13 As it is clearly seen the reconstructions for experiments performed in the transmission geometry are almost constant for the variations of the absorption coefficient.

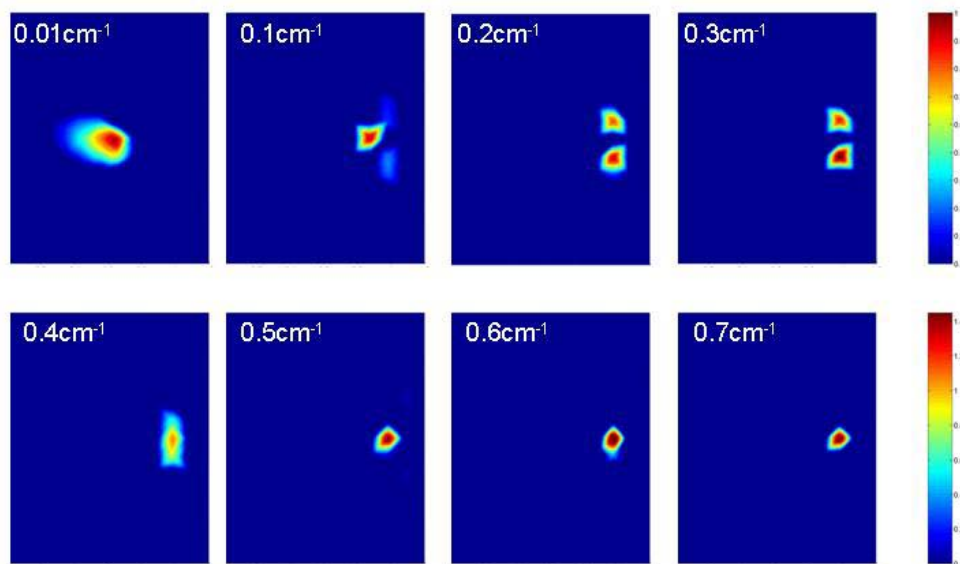


**Figure 6.12:** different reconstructions of the same data (two CFSE tubes placed at depth of 3mm, in 0.5mm distance) for different values of the absorption coefficient as an input parameter to the software, in the Reflection geometry

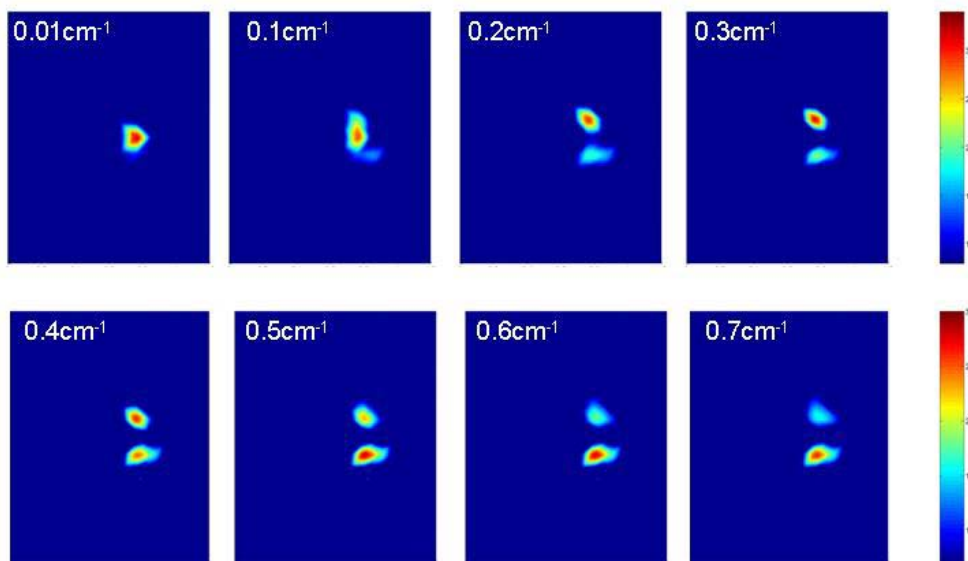


**Figure 6.13:** different reconstructions of the same data (two CFSE tubes placed at depth of 3mm, in 0.5mm distance) for different values of the absorption coefficient as an input parameter to the software, in the Transmission geometry

### 6.2.3 Spectral Unmixing

So far, we have presented the main aspects of fluorescence tomography in the case of one fluorophore located inside a turbid medium. Considering the fact that in more realistic samples (e.g. biological tissue) more than one fluorophores can be found, the following question is immediately raised: What would happen if our sample contains different fluorophores with overlapping emission spectra? Motivated by the need of finding a solution for that problem, spectral unmixing, which is a relatively new technique [29-31] has been applied.

Spectral unmixing combines two well known scientific methodologies, namely spectroscopy and imaging, to provide this advantageous tool. Apart from the fluorescence imaging already presented, we also performed spectroscopy measurements on samples containing two fluorophores (CFSE, Atto590). As it is expected the resulting fluorescence reconstruction will include signal from both probes. For this reason a simple linear algorithm is applied, in order to uncouple the two emission signals. The aim is to finally extract fluorescence reconstructions at two separate wavelength regions of interest, where only the fluorescence of one fluorophore will be present each time.

The main idea of this method is the following. Let's assume that we have a sample containing  $n$  fluorophores. In order to detect each one of them we define the detection channels which are wavelength regions where one probe emits with the higher intensity. We first measure the fluorescence signals of each fluorophore separately, determining thus their relative contribution to each detection channel, the so-called spectral strengths. We then express the reconstructed fluorescence of the FMT experiments in each channel, as a linear contribution of the  $n$  fluorescence concentrations multiplied, each one, with the corresponding spectral strength. To each detection channel corresponds one linear equation.

$$\begin{aligned}
I_1 &= s_{R1} \cdot C_R + s_{G1} \cdot C_G + \dots + s_{B1} \cdot C_B \\
I_2 &= s_{R2} \cdot C_R + s_{G2} \cdot C_G + \dots + s_{B2} \cdot C_B \\
&\vdots \\
I_n &= s_{Rn} \cdot C_R + s_{Gn} \cdot C_G + \dots + s_{Bn} \cdot C_B
\end{aligned} \quad (6.22)$$

where  $I_1, I_2 \dots I_n$  are the 3-d reconstructed images obtained from FMT in each detection channel,  $s_{Ri}, s_{Gi}, s_{Bi}$  ( $i = 1, \dots, n$ ) are the spectral strengths of each (R, G, ..., B) fluorophore in the  $i$ -detection channel and  $C_R, C_G, \dots, C_B$  are the unknown unmixed concentrations.

As it can be easily understood, this system of equations can be written in a form of matrices:

$$\begin{bmatrix} I_1 \\ I_2 \\ \vdots \\ I_n \end{bmatrix} = \begin{bmatrix} s_{1R} & s_{1G} & \dots & s_{1B} \\ s_{2R} & s_{2G} & \dots & s_{2B} \\ \vdots & \vdots & & \vdots \\ s_{nR} & s_{nG} & \dots & s_{nB} \end{bmatrix} \times \begin{bmatrix} C_R \\ C_G \\ \vdots \\ C_B \end{bmatrix} = \mathbf{S}_{ij} \times \begin{bmatrix} C_R \\ C_G \\ \vdots \\ C_B \end{bmatrix} \quad (6.23)$$

where  $S_{ij}$  ( $j=R, G, \dots, B$ ) is the relative spectral strengths matrix and the only unknown are the values of the  $C$  matrix. When the number of detection channels exceeds the number of fluorophores to be separated, the system is mathematically overdetermined and unmixing is possible. When the number of detection channels equals the number of fluorophores to be separated the system is just determined and a unique solution of the unmixing procedure is possible. This means that for two closely related fluorophores two detection channels are sufficient for efficient unmixing. Therefore it is possible to find the left-inverse matrix of  $\mathbf{S}$ ,  $\mathbf{S}^{LI}$  so that the multiplication  $\mathbf{S}^{LI} \times \mathbf{S}$  gives an identity matrix.

$$\begin{bmatrix} C_R \\ C_G \\ \vdots \\ C_B \end{bmatrix} = \mathbf{S}^{LI} \times \begin{bmatrix} I_1 \\ I_2 \\ \vdots \\ I_n \end{bmatrix} \quad (6.24)$$

Note that the  $\mathbf{S}^{LI}$  depends only on the reference spectra and can be calculated and stored before the actual measurement. The linear system of Eq.(6.3) is solved through the algorithm, resulting thus in the unmixing results.

In this section two series of experiments are presented. Firstly, the unmixing experiments of different fluorescent light inside turbid medium are presented. Results on both phantom and mice are presented. In the second part, we use the main idea of the linear unmixing for a study on the autofluorescence removal in tissue phantoms. Instead of using one excitation wavelength and recording in several detection channels, these experiments include measurements in two wavelengths and detection in one channel. This is a way to subtract the background fluorescence of our samples improving thus the quality of our results.

For the case of our experiments with the two fluorophores, small quantities of CFSE and Atto590 were inserted in the capillary tubes. The tubes were later immersed in the slab phantom. For the needs of this experiment one liquid phantom was prepared using Intralipid, agar and ink. The experiment was performed in reflection geometry, adopting a  $5 \times 13$  sources pattern over a  $16\text{mm} \times 12\text{mm}$  area and a  $24 \times 46$  detectors grid with detector size of  $1\text{mm}^2$ .

As a result, (Eq 6.2) is written as follows:

$$\begin{bmatrix} I_1 \\ I_2 \end{bmatrix} = \begin{bmatrix} s_1^{CFSE} & s_1^{Atto590} \\ s_2^{CFSE} & s_2^{Atto590} \end{bmatrix} \times \begin{bmatrix} C^{CFSE} \\ C^{Atto590} \end{bmatrix} \quad (6.4)$$

where  $I_1, I_2$  are the fluorescence reconstructions in the detection channels,  $540\text{nm} \pm 20\text{nm}$  and  $615\text{nm} \pm 45\text{nm}$  respectively,  $s_1^{CFSE}, s_2^{CFSE}$  are the spectral strengths of CFSE in the two regions and  $s_1^{Atto590}, s_2^{Atto590}$  are the spectral strengths of Atto590. These spectral regions are shown in Figure 6.14 where the fluorescence spectra of CFSE and Atto590 measured with a commercial fluorimeter are plotted against wavelength. The spectral strengths are calculated by integrating the signal under the part of the curve that corresponds to the spectral band allowed by each filter, as shown in Fig 6.14. Finally,  $C^{CFSE}$  and  $C^{Atto590}$  are the unknown reconstructed fluorescence concentrations

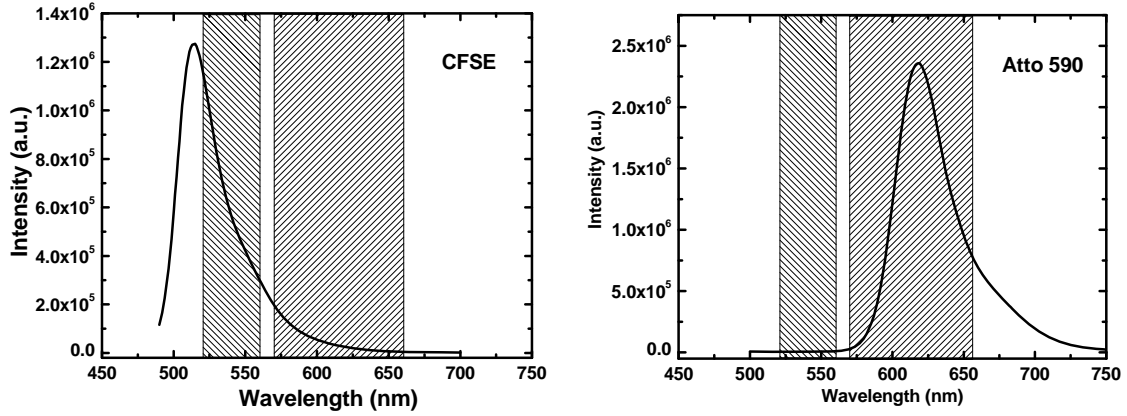


**Figure 6.14:** Fluorescence spectra of CFSE and Atto590 compared with the emission filters profiles that give the two detection channels of each fluorophore. The excitation wavelength used was the 514nm line of the Ar<sup>+</sup> laser.

The solution of the system above is given by:

$$\begin{bmatrix} C^{CFSE} \\ C^{Atto590} \end{bmatrix} = \begin{bmatrix} S_1^{CFSE} & S_1^{Atto590} \\ S_2^{CFSE} & S_2^{Atto590} \end{bmatrix}^{-1} \times \begin{bmatrix} I_1 \\ I_2 \end{bmatrix} \quad (6.5)$$

The resulting reconstructions are shown in Figure 6.15, where coronal slices of the reconstructions of the original mixed signals and the unmixing CFSE and Atto590 signals are presented after the unmixing.

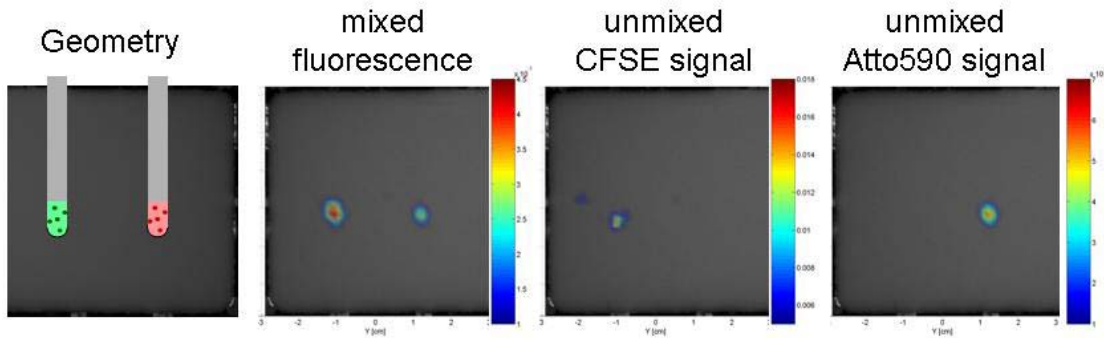


**Figure 6.15:** Reconstructed coronal slices of the mixed signals originating from the CFSE and ATTO590 tubes and the corresponding unmixed ones after we have applied the linear unmixing algorithm

A similar study was performed in vivo with a mouse, where we have implanted subcutaneously and collaterally in the upper front torso area two small capillary tubes containing 5  $\mu$ Mol of CFSE and 20  $\mu$ Mol of Atto590 respectively.

After applying the above described algorithm for the unmixing two overlapping fluorescence signals we obtain the reconstructions presented in Figure 6.16. As it is clearly seen the unmixing results are quite satisfying. The two emission signals are separated.

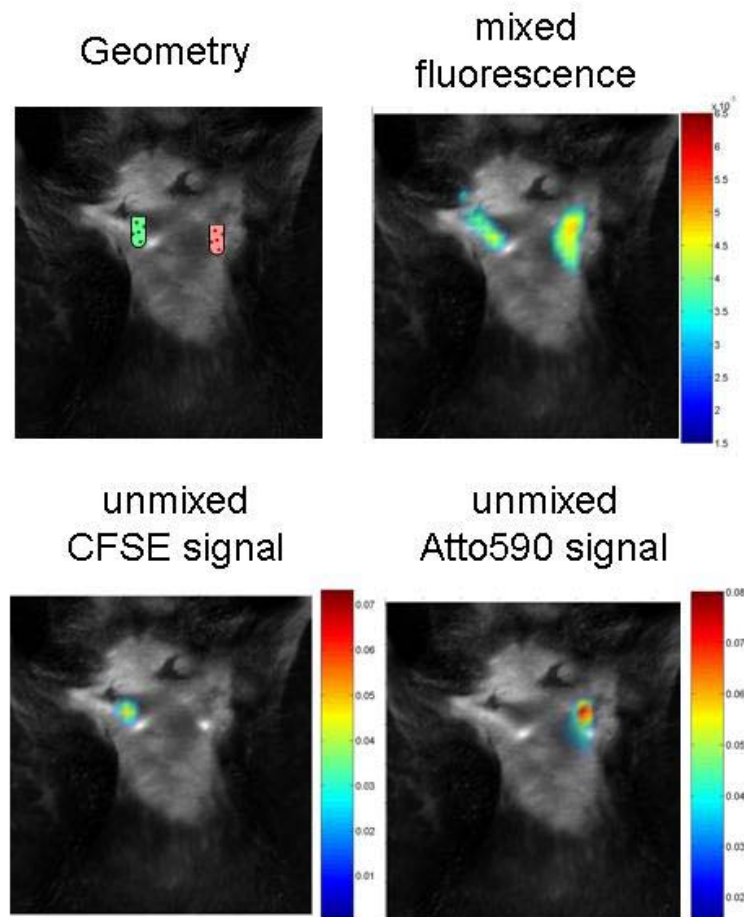


**Figure 6.16:** Reconstructed coronal slices of the mixed signals originating from the CFSE and ATTO590 tubes implanted subcutaneously and the corresponding unmixed ones after we have applied the linear unmixing algorithm

The same concept used for the linear unmixing of emission spectra can also be applied to unmixing based on the fluorophore's excitation spectra. Instead of exciting at one wavelength and collecting the emitted fluorescence into spectrally different detection channels, one can excite sequentially at different wavelengths and detect the total respective fluorescence with only one detection channel. Data acquired in such a way can then be unmixed with the same algorithm used for emission based unmixing. In this case Eq. 6.3 is written as:

$$\begin{bmatrix} C_R \\ C_G \\ \vdots \\ C_B \end{bmatrix} = \begin{bmatrix} S_{\lambda_1 R} & S_{\lambda_1 G} & \dots & S_{\lambda_1 B} \\ S_{\lambda_2 R} & S_{\lambda_2 G} & \dots & S_{\lambda_2 B} \\ \vdots & \vdots & \dots & \vdots \\ S_{\lambda_n R} & S_{\lambda_n G} & \dots & S_{\lambda_n B} \end{bmatrix}^{LI} \times \begin{bmatrix} I(\lambda_1) \\ I(\lambda_2) \\ \vdots \\ I(\lambda_n) \end{bmatrix} = \mathbf{S}^{LI} \times \begin{bmatrix} I(\lambda_1) \\ I(\lambda_2) \\ \vdots \\ I(\lambda_n) \end{bmatrix} \quad (6.6)$$

This is the procedure followed in the autofluorescence removal experiments. Tissue autofluorescence is one of the main problems of imaging in the visible. Tissue autofluorescence appears as a uniform background signal on the acquired images, especially in reflection measurements and compromises the resolution and the detection limit of the tomographic method.

In this study solid slab phantoms were employed, made by adding different concentrations of Intralipid (0%, 25%, 50%, 75% and 100%) and TiO<sub>2</sub> in a 2% agar and 0.02% India ink gel. The phantoms had approximate optical properties of  $\mu_s' = 16\text{cm}^{-1}$  and  $\mu_a = 1.5\text{cm}^{-1}$ . Inside the phantoms one capillary tube filled with 50  $\mu\text{Mol}$  CFSE was immersed at the depth of 6mm under the surface of the slab, in front of the CCD camera. The experiments were performed in reflection geometry. The illumination pattern, covering an area of 1 cm<sup>2</sup>, was comprised of 49 sources and the detection pattern had dimensions of 18mm $\times$ 18mm and the detectors' size was 1mm<sup>2</sup>. For the reconstructions, we chose a volume with dimensions 19mm $\times$ 19mm $\times$ 12mm which was discretized in 4332 mesh points. The presented reconstructions were extracted after inverting the raw data using the ART for 100 iterations. Typical times for the mapping of the fluorescence signal were of the order of 5 minutes on a 2 GHz personal computer with 1 GB RAM.

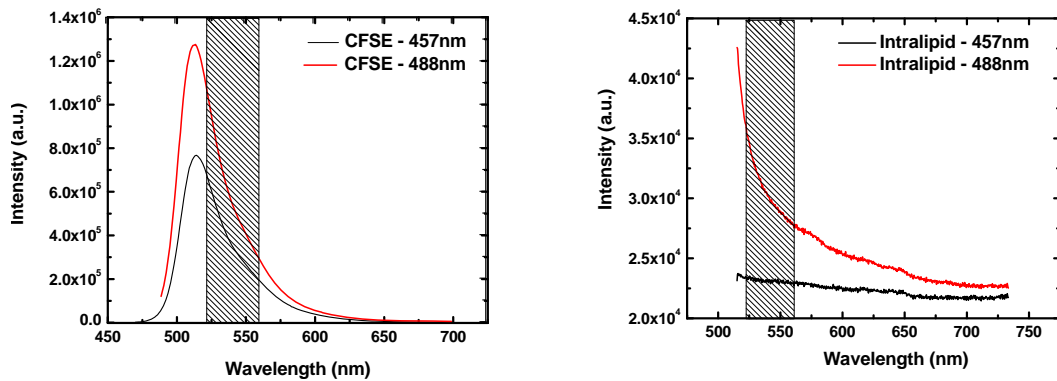


**Figure 6.17:** Emission spectra of CFSE and Intralipid when excited at 488nm and 457nm, compared with the emission filter profile that defines the detection channel

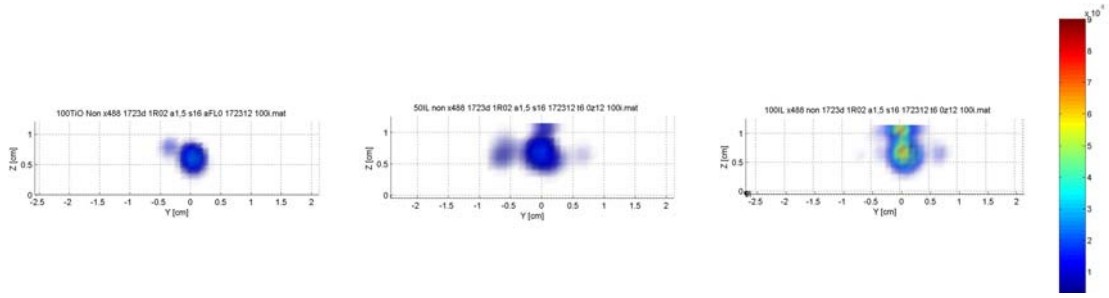


**Figure 6.18:** Reconstructions of the phantoms made by 100% TiO<sub>2</sub> (zero autofluorescence), 50% Intralipid - 50% TiO<sub>2</sub>, and 100% Intralipid, respectively.

The aim of this study was to produce different amounts of autofluorescence in a controlled way, since Intralipid is known to fluoresce when excited with blue light. Each phantom was containing a different quantity of Intralipid and as a result, a different concentration of the fluorescing material besides CFSE. The relative spectral strengths were calculated by the emission spectra of Intralipid and CFSE, acquired with our setup and shown in Fig.6.17, when excited at 488nm and 457 nm respectively. The results of this study are presented in Figures 6.19.

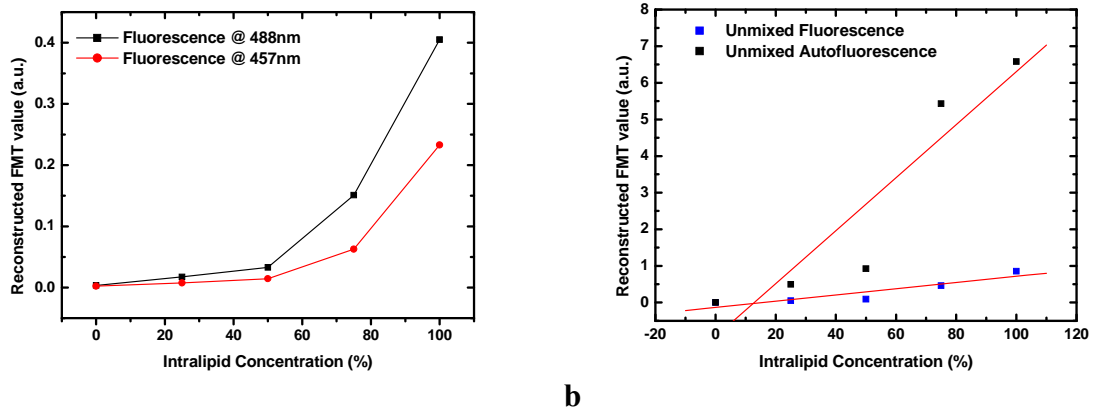


**Figure 6.19:** (a) the fluorescence reconstruction values for the different amounts of Intralipid in the slab phantoms when excited at the two wavelengths, 488nm & 457nm. (b) the unmixed fluorescence and the unmixed autofluorescence values of the reconstructions after the linear unmixing

The decomposition of the signals of CFSE and Intralipid is based on the same linear unmixing algorithm, which is applied to the reconstructed images obtained at the same spectral region for the two excitation wavelengths. The uncoupled images were calculated by solving the linear system of Eq 6.6, basically calculating the unmixed values for every voxel in the mesh, representing the volume of interest.

Autofluorescence removal is presented in Fig.6.20, where Intralipid's emission is reconstructed on the surface of the phantom, right above the reconstructed fluorescence of the CFSE tube.

After the unmixing we can see that in the autofluorescence image there is signal reconstructed in the tube's position. As it is clearly seen from the graphs of Fig.6.19, the light emission from the surrounding medium (Intralipid) affects the reconstructed signal of the tube, as the same tube is shown to have increasing fluorophore concentration. This fact leads us to the conclusion that the software accumulates the emitted signal to the center of the fluorescence source, that is, signal from the Intralipid is reconstructed in tube's position. After the decomposition we see in the graph (b) of Fig 6.19 that the CFSE fluorescence remains almost constant as compared to the autofluorescence signal which can be considered as linearly increasing. The fact that the unmixed CFSE fluorescence is slightly increasing as compared with the increasing Intralipid concentration means that the two emission signals were not completely unmixed. However the observed variation is much smaller than the respective variation of the autofluorescence signal.

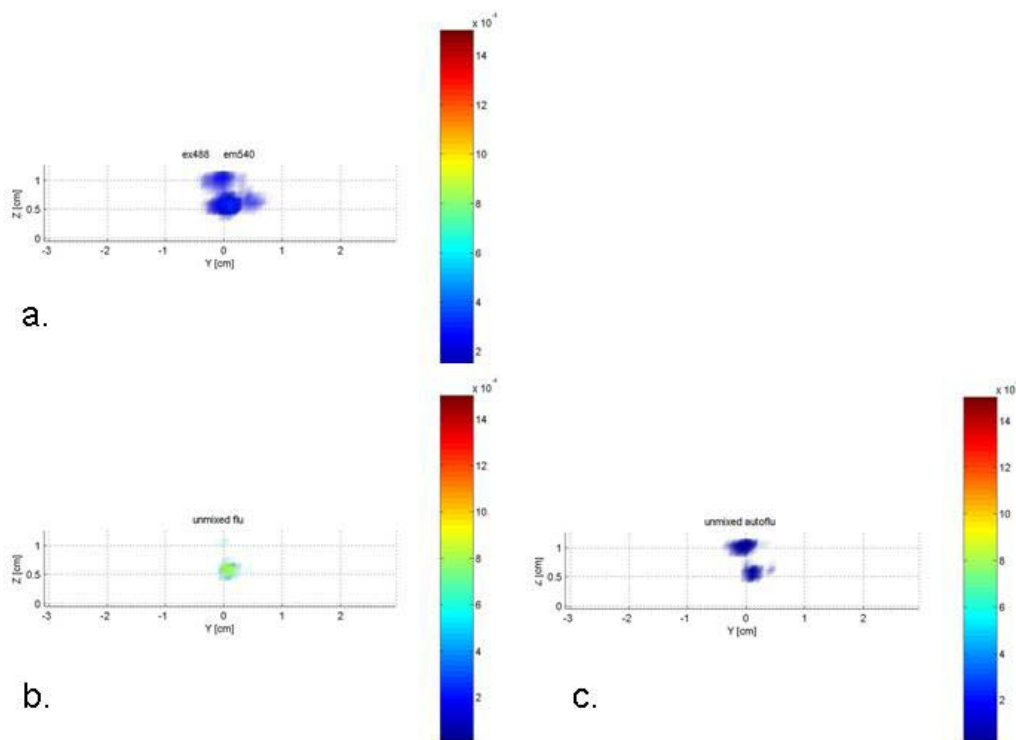


**Figure 6.20:** Autofluorescence removal was based on the same algorithm with the second spectral contribution obtained for the 457nm excitation, allowing thus the recording in only one spectral region. **a)** the mixed fluorescence signal, **b)** the unmixed fluorescence reconstruction, and **c)** the unmixed autofluorescence reconstruction

# Chapter 7

## Conclusions and future outlook

In this thesis the determination of basic characteristics of a novel 3D imaging system suitable for in vivo fluorescence molecular tomography was attempted. The aim of this work was to test the imaging system under controlled conditions, resulting thus in the standardization of the systems' main properties. In that direction, experiments with tissue-simulating objects that mimic the properties of biological tissue were performed.

Consequently, quantification experiments were performed for the two fluorophores used, in order to demonstrate the capacity of the FMT setup to quantify the different fluorescent signals inside the scattering media for both the reflection and the transmission geometry. Moreover, resolution experiments were performed by placing two tubes inside the phantom in close distance to each other trying to reconstruct their fluorescence intensities as well as their separating distance. Optical resolution describes the ability of the FMT system to detect, distinguish and reconstruct adjacent fluorescing volumes and inhomogeneities located inside the sample's volume.

A very important issue in imaging is the selection between reflection and transmission geometry. Up to now, serious constraints were posed mostly by the wavelength region of the visible that we were working in. The most of the known proteins were emitting in the visible spectrum, a region of wavelength where haemoglobin's absorption is particularly high. As a result of this light penetration inside biological tissue is in the order of a few millimetres, rendering thus the

reflection geometry as the only feasible geometry for such experiments. Great efforts are being made in the area of biotechnology for the engineering of proteins that are shifted to the red-infrared region of wavelengths. Tissue absorbance in this region is significantly low. As a result of this, light could reach deeper inside the tissue. This would also allow the use of transmission as the standard illumination geometry, further minimizing therefore the excitation of the skin autofluorescence compared to the reflection geometry.

After having performed and presented adequate number of experiments in both the reflection and transmission modes, some important characteristics are easily discerned. First of all, in both geometries the fluorophore concentrations placed at depths down to 6mm and in the distance of 0.5mm were satisfyingly detected and reconstructed. However, in the case of reflection the reconstructed images were located almost superficially, in a distance of almost 2mm under the surface, no matter what the real depth value was. On the contrary, the resulted reconstructions in case of transmission geometry are far more realistic. Nevertheless both geometries yielded positive results in the quantification linearity.

As far as this part of the thesis is concerned, in the future work would be definitely included the improving of the software in the case of reflection geometry, in order to become more depth reliable. Also, it is obvious from the results that the achievement of a distance smaller than the 0.5mm is possible in the resolution experiments. Furthermore the quantification results should also be the same between the two experimental modalities, as far as the lines' slope is concerned.

Apart from the strong absorption, another main problem of reflection imaging in the visible spectrum is tissue autofluorescence. Tissue autofluorescence appears as uniform background signal while exciting our samples. As a result autofluorescence is recorded and reconstructed reducing, thus, the resolution the detection sensitivity and the imaging performance of the FMT system in general. Autofluorescence is mostly present in measurements taken in reflection geometry. On the other hand, in the case of measurements taken with the transmission geometry background fluorescence is not so high, as it is mostly absorbed by the surrounding medium.

In that direction a method was presented for decomposing overlapping emission intensities. To that end a simple linear algorithm was applied, in order to uncouple the two emission signals. This method was used for unmixing the signal from two different fluorophores as well as for unmixing the autofluorescence from the

targeted fluorescence in phantoms and mice. As shown in the graphs, the unmixing was satisfying but not perfect as the unmixed fluorescence and autofluorescence were not fully uncoupled.

For the experiments presented in this thesis simple-structured tissue phantoms were employed. The initial aim of standardization of the FMT was demanding controlled and simple experimental conditions. However, the more complex a tissue phantom is the better it resembles its prototype, the biological tissue. In that direction, as far as the future work is concerned, more complicated phantoms can be employed. Phantoms with different layers, or fluorescing and absorbing heterogeneities immersed inside their volume would be very nice samples for further testing our system. Moreover the use of biological compatible materials such as blood and proteins' cells would also result in more realistic phantoms.

The system for fluorescence molecular tomography used for these experiments can be also used for a vast number of different experimental models, in different size scales targeting important biological processes and functions. The fact that it is capable of reconstructing three dimensional map of fluorescing volumes immersed inside turbid media, combined with the recent development of the red-shifted imaging certifies the high potential that this technique was thought to have[32]. Therefore in combination with the progress in biology, whole biological processes can be monitored and whole organs can be reconstructed. As a result new pathways have been opened for in vivo experiments and of course for the translation of the optical tomography to clinical applications.

## References

1. Ntziachristos, V., et al., *In vivo tomographic imaging of near-infrared fluorescent probes*. Mol Imaging, 2002. **1**(2): p. 82-8.
2. Ntziachristos, V., et al., *Fluorescence molecular tomography resolves protease activity in vivo*. Nat Med, 2002. **8**(7): p. 757-60.
3. Ntziachristos, V., et al., *Looking and listening to light: the evolution of whole-body photonic imaging*. Nat Biotechnol, 2005. **23**(3): p. 313-20.
4. Graves, E.E., et al., *A submillimeter resolution fluorescence molecular imaging system for small animal imaging*. Med Phys, 2003. **30**(5): p. 901-11.
5. Zacharakis, G., et al., *Volumetric tomography of fluorescent proteins through small animals in vivo*. Proc Natl Acad Sci U S A, 2005. **102**(51): p. 18252-7.
6. Zacharakis, G., et al., *Fluorescent protein tomography scanner for small animal imaging*. IEEE Trans Med Imaging, 2005. **24**(7): p. 878-85.
7. Ntziachristos, V., B. Chance, and A.G. Yodh, *Differential diffuse optical tomography*. Optics Express, 1999. **5**.
8. Graves, E.E., et al., *Validation of in vivo fluorochrome concentrations measured using fluorescence molecular tomography*. J Biomed Opt, 2005. **10**(4): p. 44019.
9. Ntziachristos, V., et al., *Visualization of antitumor treatment by means of fluorescence molecular tomography with an annexin V-Cy5.5 conjugate*. Proc Natl Acad Sci U S A, 2004. **101**(33): p. 12294-9.
10. Ishimaru, A., *Wave Propagation and Scattering in Random Media*. Vol. vol.1. 1978: Academic Press.
11. Chandrasekhar, S., *Radiative Transfer*. 1960, New York: Oxford University Press.
12. Arridge, S.R., M. Hiraoka, and M. Schweiger, *Statistical basis for the determination of optical pathlength in tissue*. Phys Med Biol, 1995. **40**(9): p. 1539-58.
13. Boas, D.A., *Diffuse photon probes of structural and dynamical properties of turbid media: Theory and Biomedical applications*. 1996, University of Pennsylvania.

14. Furutsu, K. and Y. Yamada, *Diffusion approximation for a dissipative random medium and the applications*. Phys Rev E Stat Phys Plasmas Fluids Relat Interdiscip Topics, 1994. **50**(5): p. 3634-3640.
15. Patterson, M.S., B. Chance, and B.C. Wilson, *Time resolved reflectance and transmittance for the non invasive measurement of tissue optical properties*. Appl Opt, 1989. **28**(2331-2336).
16. Aronson, R. and N. Corngold, *Photon diffusion coefficient in an absorbing medium*. J Opt Soc Am A Opt Image Sci Vis, 1999. **16**(5): p. 1066-71.
17. Ripoll, J., et al., *Kirchhoff approximation for diffusive waves*. Phys Rev E Stat Nonlin Soft Matter Phys, 2001. **64**(5 Pt 1): p. 051917.
18. O'Leary, M.A., et al., *Fluorescence lifetime imaging in turbid media*. Optics Letters, 1996. **Vol. 21**( Issue 2): p. 158-160.
19. Aronson, R., *Boundary conditions for diffusion of light*. J Opt Soc Am A Opt Image Sci Vis, 1995. **12**(11): p. 2532-9.
20. Arfken, G.B. and H.J. Weber, *Mathematical Methods for Physicists*. 4th ed. ed. 1995, New York: Academic Press.
21. Ripoll, J. and V. Ntziachristos, *From finite to infinite volumes: removal of boundaries in diffuse wave imaging*. Phys Rev Lett, 2006. **96**(17): p. 173903.
22. Ntziachristos, V., *Experimental three-dimensional fluorescence reconstruction of diffuse media by use of a normalized Born approximation*. Opt Lett, 2001. **26**(12).
23. Soubret, A., J. Ripoll, and V. Ntziachristos, *Accuracy of fluorescent tomography in the presence of heterogeneities: study of the normalized Born ratio*. IEEE Trans Med Imaging, 2005. **24**(10): p. 1377-86.
24. Kak, A.C. and M. Slaney, *Principles of computerized tomographic imaging*. 1988, New York: IEEE Press.
25. Pogue, B.W. and M.S. Patterson, *Review of tissue simulating phantoms for optical spectroscopy, imaging and dosimetry*. J Biomed Opt, 2006. **11**(4): p. 041102.
26. Durkin , A.J., S. Jaikumar, and R. Richards-Kortum, *Optically dilute, absorbing and Turbid Phantoms for fluorescence spectroscopy of homogenous and inhomogenous samples*. Appl Spectroscopy, 1993. **47**(12): p. 2114-2121
27. Tuchin, V., *Tissue Optics: Light Scattering Methods and Instruments for Medical Diagnosis*. 2000: SPIE Press.

28. Cubeddu, R., et al., *A solid tissue phantom for photon migration studies*. Phys Med Biol, 1997. **42**(10): p. 1971-9.
29. Garini, Y., I.T. Young, and G. McNamara, *Spectral imaging: principles and applications*. Cytometry A, 2006. **69**(8): p. 735-47.
30. Tsurui, H., et al., *Seven-color fluorescence imaging of tissue samples based on Fourier spectroscopy and singular value decomposition*. J Histochem Cytochem, 2000. **48**(5): p. 653-62.
31. Zimmermann, T., J. Rietdorf, and R. Pepperkok, *Spectral imaging and its applications in live cell microscopy*. FEBS Lett, 2003. **546**(1): p. 87-92.
32. Ntziachristos, V., C. Bremer, and R. Weissleder, *Fluorescence imaging with near-infrared light: new technological advances that enable in vivo molecular imaging*. Eur Radiol, 2003. **13**(1): p. 195-208.

## Ευχαριστίες

Η παρούσα διπλωματική εκπονήθηκε στο εργαστήριο της ομάδας Βιοϊατρικής Απεικόνισης του Ι.Η.Δ.Λ του Ι.Τ.Ε. στα πλαίσια του ΠΜΣ Οπτοηλεκτρονικής Μικροηλεκτρονικής. Καθώς η ολοκλήρωση της διπλωματικής εργασίας σηματοδοτεί και τη λήξη μιας σημαντικής περιόδου, και δεδομένου ότι η εργασία αυτή είναι προϊόν τόσο προσωπικής όσο και συλλογικής προσπάθειας, νιώθω την ανάγκη, στο σημείο αυτό, να ευχαριστήσω τα παρακάτω πρόσωπα.

Θα ήθελα, πρώτα απ'όλα, να ευχαριστήσω τον δρ. κ. Jorge Ripoll για την εμπιστοσύνη που μου έδειξε αλλά και την ευκαιρία που μου παρείχε να ασχοληθώ με ένα πολύ ενδιαφέρον αντικείμενο, σε ένα σύγχρονο εργαστήριο. Πέρα από τις γνώσεις, αυτά που αποκόμισα από τη συνεργασία μας ήταν πολλά και σημαντικά.

Επίσης, θα ήθελα να ευχαριστήσω τον δρ. κ. Γιαννη Ζαχαράκη για τη βοήθεια και την καθοδήγηση στα θέματα που προέκυπταν στη διάρκεια αυτής εδώ της εργασίας, είτε μέσα στο εργαστήριο είτε έξω από αυτό.

Ένα μεγάλο ευχαριστώ οφείλω στον δρ. κ. Ανίκητο Γαροφαλάκη, στους υποψήφιους διδάκτορες Heiko Meyer και Rosy Favvichio, αλλά και τους Juan Aguirre και Μαρία Σημαντηράκη. Η συνεργασία μας, οι συζητήσεις αλλά και η παρέα που κάναμε μετέτρεψαν την εργασία στο εργαστήριο σε μια πολύ ευχάριστη εμπειρία. Είναι πολύ σημαντικό στον οποιαδήποτε χώρο εργασίας το κλίμα μεταξύ των συνεργατών να είναι ευχάριστο και όχι απλώς τυπικό.

Τέλος, θα ήθελα να ευχαριστήσω την μητέρα μου Μαρία και την αδερφή μου Αλίνα για την υπομονή τους αλλά και για την αμέριστη συμπαράσταση και εμπιστοσύνη που μου δείχνουν. Βεβαίως, δεν θα μπορούσα να παραλείψω και τις ευχαριστίες μου στη Γεωργία για τη στήριξή της, και όχι μόνο, για όλο αυτό το διάστημα. Ένα μερίδιο από ό,τι έχω καταφέρει σίγουρα τους ανήκει.

Στελιος Ψυχάρκης  
Φεβρουάριος 2008